Ruthenium Metal-Organic Frameworks with Different Defect Types: Influence on Porosity, Sorption and Catalytic Properties

Wenhua Zhang,[a] Max Kauer,[a] Olesia Halbherr,[a] Konstantin Epp,[b] Penghu Guo,[c] Miguel Gonzalez,[d] Dianne J. Xiao,[d] Christian Wiktor,[a] Francesc X. LIabrés i Xamena,[e] Christof Wöll,[f] Yuemin Wang,[f]* Martin Muhler,[c] and Roland A. Fischer*[b]

Abstract: Employing the mixed component, solid solution approach, various functionalized di-topic isophthalate (ip) defect generating linkers denoted as 5-X-ipH_2, with X = OH (**1**), H (**2**), NH_2 (**3**), Br (**4**) have been introduced into the mixed-valence ruthenium-analogue of [$Cu_3(btc)_2$] (HKUST-1) to yield Ru-DEMOFs (DE = "defect-engineered") of the general empirical formula $[Ru_3(btc)_{2-x}(5\text{-X-ip})_xY_y]_n$. The framework incorporation of 5-X-ip has been confirmed by a number of techniques including PXRD, FT-IR, UHV-IR, TGA, ^{1}H-NMR, N_2 sorption as well as XANES. Interestingly, Ru-DEMOF (**1c**) with 32% framework incorporation of 5-OH-ip reveals the highest BET surface area (~1300 m^2/g, N_2 adsorption, 77 K) among all samples (including the parent framework $[Ru_3(btc)_2Y_y]_n$). The characterization data are consistent with two kinds of structural defects induced by 5-X-ip framework incorporation: type **A**, modified paddlewheel nodes featuring reduced ruthenium sites ($Ru^{\delta+}$, $0<\delta<2$) and type **B**, missing nodes leading to enhanced porosity. Their relative abundances depend on the choice of the functional group X in the defect linkers. The defects **A** and **B** appeared also to play a key role in sorption of small molecules (*i.e.*, CO_2, CO, H_2) as well as for the catalytic properties of the samples (*i.e.*, ethylene dimerization and Paal-Knorr reaction).

[a] W. Zhang, Dr. O. Halbherr, M. Kauer, Dr. C. Wiktor,
Chair of Inorganic Chemistry II, Ruhr University Bochum,
Universitätsstraße 150, 44801 Bochum (Germany)
[b] K. Epp, Prof. Dr. R. A. Fischer
Chair of Inorganic and Metal-Organic Chemistry
Technical University Munich,
Lichtenbergstraße 4, D-85748 Garching (Germany)
E-mail: roland.fischer@tum.de
[c] P. Guo, Prof. Dr. M. Muhler
Laboratory of Industrial Chemistry
Ruhr University Bochum (Germany)
Universitätsstraße 150, 44801 Bochum (Germany)
[d] M. Gonzalez, D. J. Xiao
Department of Chemistry, University of California, Berkeley
Berkeley 94720 California (USA)
[e] Dr. F. X. LIabrés i Xamena
Instituto deTecnología Química (ITQ)
Universitat Politècnica de València
Consejo Superior de Investigaciones Científicas
Avenida de los Naranjos s/n, 46022 Valencia (Spain)
[f] Prof. Dr. Ch. Wöll, Dr. Y. Wang
Institute of Functional Interfaces (IFG)
Karlsruhe Institute of Technology (KIT), Karlsruhe (Germany)
E-mail: yuemin.wang@kit.edu
Supporting information for this article, including detailed experimental protocols, elemental analysis, PXRD, TGA, NMR, IR, EDX, XANES, XPS, UHV-IR and gas sorption data (N_2, CO, H_2, CO_2), is given via a link at the end of the document.

Introduction

Metal-organic frameworks (MOFs), constructed from metal ion nodes and organic linkers, have been studied in a number of fields including gas sorption[1], gas separation,[2] catalysis,[3] sensing,[4] and drug delivery.[5] Recently, it has been recognized that MOFs, similar to other (crystalline) solid-state materials, are typically not perfect crystals with infinite periodic repetition or ordering of the identical groups of atoms in space. In fact, defects of various types and length scales (even more generally: structural heterogeneity) cannot be rigorously avoided during synthesis and crystal growth and often play an important role for the material properties.[6] The diversity of MOF structures connected with the issues of intrinsic and intentional structural defects, non-stoichiometry and heterogeneity suggests a much broader approach for understanding and tailoring their chemical and physical properties.[7] Ravon and co-workers reported Zn-MOFs, featuring defects as acid active catalytic centers (generated through fast precipitation or partial linker substitution) that are responsible for shape selectivity in alkylation of large aromatic molecules.[8] Vermoortele *et al.* demonstrated generation of defects in UiO-66(Zr) *via* the coordination modulation approach.[9] As a result, better catalytic performance in several Lewis-acid catalyzed reactions was observed for the "defect-engineered" MOF. Recently, a direct correlation was found to exist between the concentration of missing linker defects in UiO-66 and its catalytic activity for the acid-catalyzed esterification of levulinic acid with alcohols.[10] Controlled introduction and characterization of specific defects into MOFs is quite a challenge including the comparison with the parent (more or less) "defect-free" reference samples.

$[Cu_3(btc)_2]_n$ (also known as HKUST-1)[11] as well as the isostructural family $[M_3(btc)_2]_n$ (M = Mo,[12] Cr,[12b, 13] Ni,[12b, 14] Ru,[12b, 15] Zn,[12b, 16], btc = benzene-1,3,5-tricarboxylate) attracted considerable attention over last years, mainly due to coordinatively unsaturated metal-sites (M-CUS), which could be readily available after appropriate post-synthetic treatment. Intentional defect generation in $[Cu_3(btc)_2]_n$ was initially reported by Baiker *et al.* who studied partial replacing of btc by the homologous pyridine-3,5-dicarboxylate (pydc) linker and revealed enhanced catalytic activity of the modified MOF in the oxidation of benzene derivatives related to modified coordinatively unsaturated sites (M-CUS) at the nodes.[17] Subsequently, we have demonstrated that not only pydc, but also a series of other defect generating linkers can be framework incorporated in case of $[Cu_3(btc)_2]_n$.[18] Interestingly, functionalized mesopores along with the M-CUS appeared to be generated in such defect-engineered MOFs (DEMOFs). In parallel, Hupp *et al.* gave an account of the enhanced porosity by introducing isophthalate (ip) into $[Cu_3(btc)_2]_n$.[19] The concept of defect engineering by a mixed component approach using

fragmented linkers together with the parent one was also expanded to the isostructural Ru-analogue.[20] Ru-DEMOFs $[Ru_3(btc)_{2-x}(pydc)_xY_y]_n$ (Y = counter-ion, Cl^-, OH^-, OAc, etc.; 0 < y ≤ 1.5) were obtained through direct mixing of H_2pydc and H_3btc in one-step solvothermal synthesis. The generation of reduced $Ru^{\delta+}$ (0<δ<2) sites at the paddlewheel nodes as a consequence of defect linker incorporation was correlated with enhanced CO uptake as well as improved catalytic activity in olefin hydrogenation. Remarkably, low temperature (100 K) dissociative chemisorption of CO_2 leading to coordinated CO was observed by UHV-FTIR spectroscopy in the dark. However, regardless of the obviously more advanced properties as compared with the parent material, the actual compositions of these Ru-DEMOFs are very difficult to establish and are not entirely clear. This stems from the structural complexity of such multi-component solid solution MOFs and a range of possible compositional variations need to be taken into account, which are not mutually exclusive (counter-ions, residual synthesis components such as linkers, coordination modulators etc.).

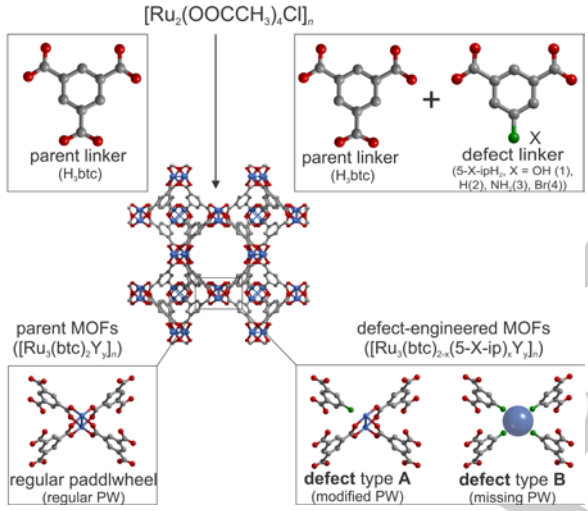

Figure 1. Design concept of the Ru-DEMOFs applying the mixed component/fragmented linker solid solution approach and sketch of the two possible, most important paddlewheel-node related defects.

Figure 1 summarizes the concept of defects introduction into mixed-valence $[Ru_3(btc)_2Y_y]_n$ by using divalent isophthalate linkers as fragmented variants of trivalent btc. Mainly, two types of defects need to be distinguished: Type **A** refers to structurally and electronically modified paddlewheel units (missing one carboxylate ligator function), in which (at least) one out of the four bridging carboxyl groups from the parent btc linker in the regular paddlewheels has been partly substituted by the (neutral) functional group of the defect linker. Consequently, for charge compensation, the metal sites could be either partly reduced (mixed-valence state) or may carry additional anionic (mono-valent) ligands (Y)[7, 20] However, apart from such type **A**, defects of type **B** could be formed, where whole paddlewheel nodes are eliminated from the structure, as it has been demonstrated in the case of ip introduction into $[Cu_3(btc)_2]_n$.[19] It is conceivable, that such missing node defects could be formed in a correlated fashion during the MOF crystal growth process and in such a case larger areas of missing nodes may be generated to yield mesopores. Being mainly studied in Cu-HKUST-1, a comprehensive understanding of the nature and formation of different types of isolated local and larger scale correlated defect sites in DEMOFs of the $[M_3(btc)_2]_n$ family and MOFs in general is very limited and this research is still at its infancy.[7] Herein, we follow-up our previous investigations on defect engineering in $[Ru_3(btc)_2Y_y]_n$ using H_2pydc as (single) defect generating linker.[20] Similar to our previous more elaborate study on defect-engineered Cu-HKUST-1[18], we now selected a series of 5-X-isophthalic acids (5-X-ipH_2, X = OH, H, NH_2, Br) and mixed them with H_3btc to yield the Ru-DEMOFs of the general formula $[Ru_3(btc)_{2-x}(5\text{-X-ip})_xY_y]_n$ (Figure 1). A number of complementary characterization methods were applied to obtain compositional and microstructure data of the materials. The aim was to at least qualitatively assess the tendency of type **A** and type **B** defect formation as a function of synthetic conditions and the chosen 5-X-ip linker. Several catalytic reactions, such as ethylene dimerization and Paal-Knorr reaction (usually running under Lewis acidic conditions) as well as low temperature $CO_2 \rightarrow CO$ dissociative chemisorption in the dark under UHV conditions, have been chosen as test reactions to monitor the influence of defects on the performance of the Ru-DEMOFs.

Results and Discussion

In the following, we provide a comprehensive account on the conducted experiments, obtained analytical and characterization data for elucidation of the defect structure of Ru-DEMOFs of the general formula $[Ru_3(btc)_{2-x}(5\text{-X-ip})_xY_y]_n$. The main goal of our presented study is to substantiate the hypothesis of type **A** and type **B** defect formation in these systems as introduced above (Figure 1). Due to the amount of collected information on the systems, only the most significant data have been selected for display in Figures and Tables in the main text. In order to save space for concise discussion, we moved most of the systematic data documentation to the supporting information.

Synthesis and characterization of the Ru-DEMOF materials (1a-d, 2a-d, 3a-d, 4a-c)

All Ru-DEMOF samples were obtained according to the previously published procedure,[20] using $[Ru_2(OOCCH_3)_4Cl]_n$, H_3btc and defect generating 5-X-ipH_2 as starting materials in the acetic acid/water solution under solvothermal conditions. The sample-numbering scheme is based on the framework incorporated 5-X-ip linker: X= OH (**1**), H (**2**), NH_2 (**3**) or Br (**4**). Further labeling (**a**, **b**, **c** etc.) refers to various levels (molar%) of defect linker incorporation. The PXRD patterns of the as-synthesized and activated samples indicate that all materials (except **2d**) are crystalline and isostructural with the parent Ru-MOF that is obtained employing the same method with H_3btc, only (Figures S1 and S2). It should be noted that $Ru^{2+/3+}$ ions can be easily reduced to eventually yield metallic ruthenium. Therefore, the solvothermal synthesis conditions have to be carefully monitored. However, no PXRD-peaks in the 2θ range of 40-45° were found, neither for the as-synthesized nor for the activated samples, thus suggesting the absence of a substantial amount of Ru^0-nanoparticles (Ru-NPs). Reflections at 42.1° and 44° are usually assigned to (001) and (101) faces of hexagonal

close-packed metallic Ru-particles or Ru-NPs.[21] We will describe further characterizations, XANES in particular, below. The corresponding results provide additional evidence for the absence of Ru/RuO_x-NPs in the obtained Ru-DEMOFs.

With the exception of **2d**, thermal gravimetric analysis (TGA) shows no decomposition of the prepared materials for temperatures below 250 °C, suggesting that thermal stability of Ru-DEMOFs is preserved as compared to the parent MOF (Figure S3). The incorporation and quantification of defect linkers have been initially testified by NMR spectroscopy of the digested samples after activation and the assessment of porosity (Table S2). Thus, in the ^{1}H-NMR spectra of the samples **1a-d,** appearance of two additional peaks (compared with the parent Ru-MOF) at 7.51 ppm and 7.89 ppm is clearly seen (Figure S4). These two resonances can be assigned to the aromatic protons of 5-OH-ip linkers. Expectedly, upon increasing the feeding amount of the defect linker (5-OH-ipH_2), the intensities of its characteristic resonances also increases in the digested sample solution (Figure S4). A similar scenario was observed also for the samples with ip defect linker (series **2a-c**). Resonances corresponding to the protons of ip are seen at 8.4 ppm, 8.1 ppm and 7.6 ppm (Figure S5). The framework incorporation amount of ip in **2a-c** increases upon increasing the concentration of the defect linker in the reactant solutions. However, the incorporated amount of ip was found to be higher than expected from the H_3btc:H_2ip feeding ratio, which is in contrast with that in the case of Ru-DEMOF series **1** where the incorporation of 5-OH-ip stay the same (or a little less) than the feeding concentration in the starting reactants. This result might be attributed to the slightly different coordination equilibria that correlate with the Brønsted acid dissociation constants of the used linkers: pKa (H_3btc) = 3.12, 3.89, 4.70 and pKa (H_2ip) = 3.46, 4.46.[22] However, the pKa differences are small and a conclusive explanation based on pKa is not straightforward. Dincă *et al.* argued that deprotonated btc could serve as a counter-ion to provide the charge balance of $[Ru_2]^{5+}$ units in Ru-analogue of Cu-HKUST-1.[12b] From our earlier investigation we concluded that H_3btc is present in the pores of $[Ru_3(btc)_2Y_y]_n$ in the form of fully protonated species, rather than as deprotonated counter-ions.[23] Both studies indicate that the linker used for the synthesis could still be present in the obtained materials. Hence, it is conceivable that the defect generating H_2ip linker can also reside either as a counter-ion or as a guest molecule in the pores of the Ru-DEMOFs (**2a** and **2b**). On the basis of these arguments it can be understood why the amount of incorporated ip can be higher than expected from the H_2ip:H_3btc feeding ratio. Indeed, very weak IR-bands in the range of ν(C=O), ν(C=C) or ν_{as}(COO) vibrations (1736-1521 cm^{-1}) have been observed in case of samples **2a-2d**. However, the small separation of the ν(C=O) bands of non-coordinated acetic acid (1715-1640 cm^{-1}),[24] protonated/non-coordinated H_2ip (1670 cm^{-1}) and H_3btc (1680 cm^{-1}) (see Figure S8) makes it hard to unambiguously determine the exact origin of these weak vibrations.

Here it should be pointed out that in all ^{1}H-NMR spectra of the digested Ru-DEMOF samples the resonance at ca. 1.91 ppm, originated from the –CH_3 groups of acetate, has been detected. This is in line with our previous investigations on the parent single-linker Ru-MOFs obtained from various Ru-precursors and the Ru-DEMOFs with pydc defect linker, where the same resonance due to acetate in the digested samples with the molar ratio of n(AcO):n(btc) in the range from 0.7 to1.8 was always observed as well.[20, 23]. We anticipate three main origins of the presence of acetate in the discussed Ru-MOFs: i) it may act as a counter-ion to compensate the overall charge of the framework (Figure S7a); ii) owing to the competition with btc and 5-X-ip, it could be residual/non-substituted and paddle wheel coordinated acetate-groups of the used Ru-precursor ($[Ru_2(OOCCH_3)_2Cl]_n$) (Figure S7b); iii) finally, it might reside as AcOH in the pores of the framework through weak interactions and, therefore, cannot be easily removed by washing and subsequent thermal activation (*i.e.,* heating at 150 °C under dynamic vacuum). To recall, the glacial acetic acid/water mixture (AcOH:H_2O = 0.05:1) was found to be essential for a successful synthesis and was always used for all reported Ru-(DE)MOFs (see Experimental Section). Besides, employed linkers may also serve as guest molecules as has been mentioned above. Attempts to evaluate the presence of acetic acid and linkers from the IR spectra is not quite feasible due to the overlapping of the bands of ν_{as}(COO) and ν_s(COO) (coordinated in a bidentate-bridging mode and free-coordinated carboxylate group)[25] as well as low intensity of the respective bands. Although one can monitor acetate groups in IR-spectroscopy by employing F-labled acetate (eg. perfluoro-acetate instead of acetate) for synthesis,[26] the crucial synthesis parameters of Ru-MOFs make this attempt impossible. Earlier effort of using various acids as the reaction solvent failed to form crystalline parent Ru-MOF.[23] Consequently, the presence of acetate (mainly) and non-reacted free linkers used in Ru-DEMOFs raises questions about the actual sample compositions and local structures and, thus, causes more complications with ambiguous interpretation of the analytical data than in case of the homologous Cu-DEMOFs.[18] The compositions of the Ru-DEMOFs samples discussed in this work have been derived by taking into account the complete set of experimental results and a full account is given in the Supporting Information (Tables S3 and S4). As quantitative digest of the samples **3a-d** is not sufficient, detection and determination of the defect linker contents (5-NH_2-ip) from ^{1}H-NMR measurements was not possible. Nevertheless, the IR spectra of these samples provide a qualitative evidence for the 5-NH_2-ip incorporation. Indeed, the observed bands at 1651 cm^{-1} and 1264 cm^{-1} stem from δ(N-H) and ν(C-N) vibrations of the 5-NH_2-ip (Figure S8). In case of the 5-Br-ip (samples **4a-c**), the gradual increase of intensities of the respective signals in both ^{1}H-NMR and TEM-EDX spectra suggests the presence of defect linker in these Ru-DEMOFs (see Figures S6 and S9).

To support further the framework incorporation of the defect linker and rule out its extra framework inclusion within the pores in a high quantity, we have carried out N_2 sorption measurements for the activated samples. The N_2 sorption isotherms at 77 K for all samples (**1a-d, 2a-d, 3a-d** and **4a-c**) reveal type I isotherm without any hysteresis loop (Figure S10), indicating that all Ru-DEMOFs are microporous materials.[27] In general, while comparing with the Brunauer-Emmett-Teller (BET) surface area (S_{BET}) of the parent Ru-MOF (998 m^2/g), one can consider Ru-DEMOFs being analogous when the value (S_{BET}) is in/above the range of the parent one. In other words, the considerably high S_{BET} of the discussed Ru-DEMOFs rules out substantial guests occlusion and pore blocking such as by non-reacted defect linkers, acetate or Ru/RuO_x-NPs. Interestingly, when 5-OH-ipH_2 is used as defect linker, S_{BET} of the Ru-DEMOFs gradually increases until 5-OH-ip is incorporated up to 32% (**1c**) (Figure 2). Notably, the S_{BET} of this

sample **1c** is the highest among all $[Ru_3(L)_2Y_y]_n$ isostructural MOFs (including the single-linker and other mixed-linker Ru-DEMOFs reported so far).[15a, 20] This indicates that the 5-OH-ip is a good candidate for defects engineering in Ru-MOFs. To remark, for comparison of the obtained S_{BET} values for Ru-MOFs with the homologous Cu-MOFs, it might be more informative using m^2/mmol units (due to substantial difference in the molecular weight of Cu and Ru). Thus, as could be seen from Table S6, the S_{BET} of the parent Ru-MOF (964 m^2/mmol) is quite similar to that of a typical reference sample $[Cu_3(btc)_2]_n$ (1049 m^2/mmol). More importantly, the S_{BET} of the Ru-DEMOF solids slightly increases in comparison with both parent analogues.

In contrast with the Ru-DEMOFs series **1**, the integration of the ip defect linker generally results in lower porosities, as demonstrated by the results for samples **2a-2d**. However, the S_{BET} of samples **2a** and **2b** are still higher than the S_{BET} of the parent Ru-MOF. Nonetheless, upon increasing the ip content, the surface area decreases. Thus, considering porosity characteristics, the optimum incorporation extent of defect linker in these series stays at 28% (sample **2b**). In case of 5-NH_2-ip defect linker, the porosity of the **3a-c** Ru-DEMOFs is fully maintained, while increasing of the feeding level to 50% leads to porosity decrease instead (sample **3d**, S_{BET} = 781 m^2/g). These observations in **2a-d** and **3a-d** series are probably due to the accommodation of unreacted 5-X-ipH_2 in the pores. Along with the increasing feeding of 5-X-ipH_2 the competition between btc and 5-X-ip increases. Subsequently, it is more difficult to rule out the presence of unreacted 5-X-ipH_2 as the reason of the decreasing S_{BET}. In the same line of reasoning, the S_{BET} of the samples **4a-c** dramatically decreased from 996 to 693 m^2/g. Hence, the optimized incorporation of 5-Br-ip can only reach up to 17% (**4a**). Notably, in our previously studies on the defect-engineered Cu-HKUST-1, the generation of mesopores was observed.[18] Curiously, in the present case of the homologous Ru-DEMOFs, we notice an opposite trend that might be attributed to the preference of isolated defects rather than to the correlated defects in the framework (Figure S11).

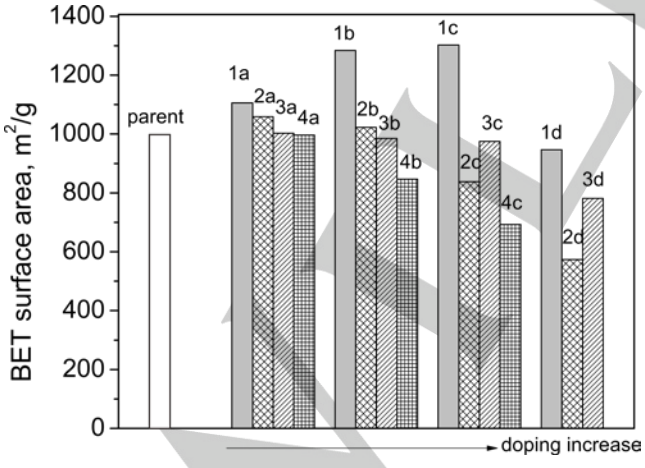

Figure 2. The variation of the BET surface area (S_{BET}) derived based on measured N_2 sorption isotherms (77 K) upon increase of the defect linker doping. 'Parent' stands here for parent single-linker Ru-MOF (with only btc). In the samples **1a-1d** 5-OH-ip serves as a defect linker; **2a-2c** – ip; **3a-3d** – 5-NH_2-ip; **4a-4c** – 5-Br-ip, respectively.

XANES, XPS and UHV-FTIR studies: ruthenium oxidation state variation as indication of defect type formation

As earlier mentioned, in our previous studies on doping of the Ru-MOF with defect pydc linker, we have assigned the introduced local defects, according to Baiker *et al.*,[17] as modified Ru-paddlewheels with three coordinating btc and one pydc linker, in which the pyridyl-N site acts as a weakly binding ligator-site over the Ru-dimer. Such structural irregularities are associated with (partially) missing linker function (*i.e.*, carboxylate) and consequently steric and electronic modification of the Ru-SBUs (see Figure 1). Additionally, partial ruthenium reduction has been observed. Namely, apart from the expected Ru^{2+} and Ru^{3+} (as in the parent Ru-MOF), we revealed also distinctly reduced framework Ru-species ($Ru^{\delta+}$, $0<\delta<2$) in the pydc-doped Ru-DEMOFs.[20] Since pydc is a divalent (anionic) linker of one charge less than btc, charge compensation by reduction of some Ru-ions may take place (in the absence or in parallel of other charge compensating effects such as accommodating additional Y anions). Note, we reported also the significant formation of mixed-valence Cu^{2+}/Cu^{1+} paddlewheels for the related pydc-doped Cu-HKUST-1 material.[18] Interestingly, in parallel studies on isostructural Cu-HKUST-1, doped with ip (rather than pydc and other 5-X-ip), predominantly defects **B** (see Figure 1) and no significant change of the copper oxidation state were reported.[19] Thus, the choice of the defect generating linker in combination with type of the metal and the synthetic conditions (doping level) most likely defines the types of defects induced in the particular type of MOF structure. Therefore, we were interested to investigate the oxidation state of the Ru-centers in the series with 5-X-ip defect linkers (X = OH, H, NH_2 and Br) in comparison with our previous data on the pydc-case,[20] and further, to confirm the assignment of the defect types.

XANES spectra (Figure S12) show deviation of the edge jump derivative for the samples **1a-d** from that one of the parent Ru-MOF. For **1a-c**, the position of edge jump gradually shifts to the lower energies, suggesting reduced Ru-sites with oxidation states lower than 2+ or 3+. We relate this observation to the generation of defects **A** in the samples **1a-c**. However, the position of the edge jump in case of the sample **1d** moved again to higher energies, illustrating that the amount of reduced Ru-species is now decreased with respect to samples **1a-c**. The different tendency suggests that defects of type **B** may also be created when 5-OH-ip linker was incorporated into the framework at ratios higher than 32%. The same trend has been observed for the 5-NH_2-ip linker (samples **3a-c**). Indeed, the XANES spectra of the samples **3a**-**b** suggest again the presence of reduced $Ru^{\delta+}$ ($0<\delta<2$) sites, but the oxidation state of the Ru-centers in **3c** is the same as in the parent Ru-MOF (Figure S14). Furthermore, when the 5-Br-ipH_2 defect linker is employed, the oxidation state of Ru is varied as well (in particular sample **4a**, Figure S15). These data support the assignment of locally modified node defects **A** for these samples. Interestingly, the position of the edge jump in case of the ip-doped samples **2a-b** does not change compared with that in the parent Ru-MOF (Figure S13). The Ru oxidation state is not affected by the incorporation of ip, which could be taken as indication of a predominance of defects of type **B** for samples **2a-b**. When the functional group of the defect linkers changes from small, coordinative inert H to the somewhat larger and coordinative

more suitable ligator-sites like -OH, -NH_2 or -Br, the defects of type **A** are favored in case of relatively low doping level. However, upon rising the doping level, defects **B** are increasingly created along with some remaining defects **A**, resulting in less pronounced variation of the oxidation state of Ru in the defect-engineered samples compared with the parent material.

It is important to note that the curve of XANES spectra (normalized absorption *vs.* energy, Figure S16) of all the Ru-DEMOFs samples as well as the parent Ru-MOF are strikingly different from those measured for the Ru-NPs, metallic Ru and RuO_2. These observations support PXRD results (see above and Figures S1 and S2, SI) and allow also to rule out the presence of other Ru-phases as significant impurities in the Ru-DEMOFs including parent Ru-MOF.[21] Thus, we assume that it is valid to assign all Ru-species to the metal-nodes of the frameworks. Further information on the local environment of Ru can be obtained also from EXAFS. The analysis of the experimental data is, however, a formidable effort, since many different models for Ru-DEMOFs have to be considered. Therefore, a thorough analysis of the EXAFS-data is outside the scope of this paper.

The different samples fabricated in this study have also been characterized using High-resolution X-ray photoelectron spectroscopic (XPS) in order to confirm the assignments based on XANES and for a more quantitative estimation of the relative abundance of the different Ru-species (Ru^{3+}, Ru^{2+} and $Ru^{\delta+}$) in the Ru-DEMOFs. The samples **1a, 1c, 1d, 2a** and **2b** with 5-OH-ip and ip defect linkers, respectively, have been selected. Remarkably, similar to the related pydc-doped Ru-DEMOFs we elaborated earlier,[20] reduced $Ru^{\delta+}$-species have been found in the Ru-DEMOFs (samples **1a, 1c** and **1d**) in addition to the Ru^{2+}- and Ru^{3+}-species. Two Ru 3d doublets ($3d_{5/2}$ and $3d_{3/2}$) at ca. 281.6 and 285.8 eV as well as at 282.6 and 286.8 eV, attributed to the Ru^{2+}- and Ru^{3+}-species, respectively, are seen in the deconvoluted XP spectra of all measured samples (Figure 3). In addition, another Ru 3d doublet appears at ca. 280.5 and 284.7 eV in the Ru-DEMOFs samples **1a, 1c** and **1d**. On the basis of quantitative estimations of the XP spectra, some variation of the Ru^{3+}/Ru^{2+} ratio and, in particular, reduction to $Ru^{\delta+}$ in **1a, 1c** and **1d** can be clearly seen (Table S6). From the parent Ru-MOF to the Ru-DEMOF sample **1a**, the ratio of Ru^{3+} / Ru^{2+}/ $Ru^{\delta+}$ varies from 1 / 1.24 / 0 to 1 / 1.75 / 0.08, indicating that the incorporation of defect linker induces partial ruthenium reduction (*i.e.*, relative concentrations of the Ru^{2+} and $Ru^{\delta+}$ increase). Moreover, upon increasing the incorporation level of 5-OH-ip to 32% for **1c** (feeding level 30%), the amount of the reduced $Ru^{\delta+}$-species considerably increases to the highest value (Ru^{3+} / Ru^{2+}/ $Ru^{\delta+}$ = 1 / 1.69 / 0.59) among all studied samples. Importantly, the $Ru^{\delta+}$-related doublet decreases significantly in intensity with further increase of the incorporation to 37% for **1d** (feeding level 50%). This is in contrast to the observation for pydc-doped Ru-DEMOFs, where a continuous rise of the $Ru^{\delta+}$ signals was detected along with increasing degree of pydc incorporation.[20] The relatively lower concentration of Ru^{2+} and $Ru^{\delta+}$ in **1d** (Ru^{3+} / Ru^{2+}/ $Ru^{\delta+}$ = 1 / 1.23 / 0.09), as compared to the respective ratios estimated for **1c**, can be explained by our assumption of simultaneous generation of both defects **A** and **B** with distinct preference of **B** over **A** at higher feeding concentrations of 5-OH-ip. Interestingly, for the ip-doped samples **2a-b** no highly reduced $Ru^{\delta+}$ have been observed in the XP spectra (no Ru3d doublets at ca. 280.5 and 284.7 eV; Figure 3). These data confirm the assignment deduced from XANES data, suggesting that application of defect linker with the coordinatively inactive functional group H (**2a-b**) is likely to more selectively induce missing node defects **B** in the Ru-DEMOFs without Ru reduction (as this is indicative for a type **A** defect). According to the results of XANES and XPS, we thus conclude that the Ru-DEMOFs materials with 5-X-ip (X= OH, NH_2 and Br) contain predominantly defects of type **A**, especially at moderate incorporation levels. However, the simultaneous generation of defects **B** in these samples is also likely as indirectly deduced from the non-linear dependence of the XANES and XPS data on the doping level.

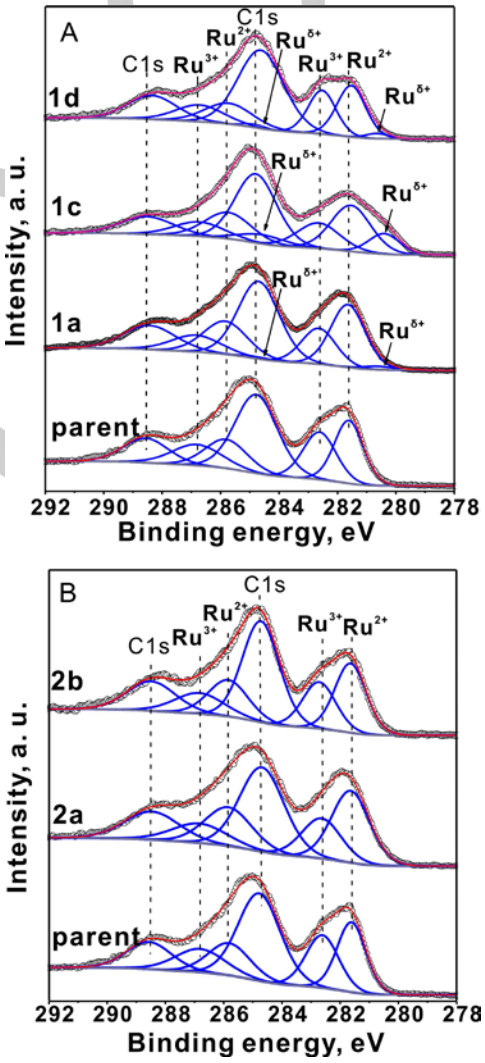

Figure 3. Deconvoluted XP spectra of the Ru-DEMOFs samples (A)**1a** (8% of 5-OH-ip), **1c** (32% of 5-OH-ip) and **1d** (37% of 5-OH-ip), (B) **2a** (15% of ip) and **2b** (28% of ip) in Ru 3d and C 1s regions in comparison with parent Ru-MOF.

Consequently, UHV-IR spectroscopic investigations employing CO as a probe molecule have been carried out on two representative samples **1c** and **1d** to gain complementary evidence on the valence states of framework Ru sites and the associated defect types. Parent Ru-MOF was reported to reveal bands at 2172 and 2127 cm^{-1}, arising from CO interactions with Ru^{3+} and Ru^{2+}, respectively (Figure S18).[20] Apart from these

two bands, the spectra of the samples **1c** and **1d** show additional bands at 2041 and 1998 cm^{-1}, which can be attributed to CO bound to reduced $Ru^{\delta+}$ ($0<\delta<2$) and again indicate the presence of defects **A** (*i.e.*, modified paddlewheels). Notably, the relative intensity of the band at 2171 cm^{-1} (Ru^{3+}) decreases largely as compared to the parent Ru-MOF, which is associated with the generation of reduced $Ru^{2+/\delta+}$ species. On the other hand, increasing the doping of 5-OH-ip from 32% (**1c**) to 37% (**1d**) leads to a significant attenuation of the CO bands associated with Ru^{2+} (ca. 2127 cm^{-1}) and $Ru^{\delta+}$ (ca. 2041 and 1998 cm^{-1}), whereas for pydc-doped Ru-DEMOFs the abundance of reduced $Ru^{\delta+}$ increases gradually upon increasing the amount of pydc.[20]. These findings confirm again the coexistence of defects **A** and **B** in Ru-DEMOFs at relatively high degree of 5-OH-ip incorporation (**1d**). The formation of defect **B**, namely missing Ru-paddlewheels, is accompanied by lowering the abundance of Ru^{2+} and $Ru^{\delta+}$ metal centers in the framework, which explains the observed changes of the decreased intensity of Ru^{2+} and $Ru^{\delta+}$ in the sample **1d**.

In our earlier report on pydc-doped Ru-DEMOFs, we communicated on the low temperature $CO_2 \rightarrow CO$ dissociative chemisorption under UHV conditions in a dark environment, a feature which is not inherent for the parent Ru-MOF.[20] We concluded that the $CO_2 \rightarrow CO$ reduction might be triggered by the reduced $Ru^{\delta+}$-sites and the pyridyl N-sites in the proximity of the modified Ru-centers at the nodes. In order to confirm these assumptions further, we have studied the same reaction at Ru-DEMOFs that feature reduced $Ru^{\delta+}$-sites. As these sites have been created by the incorporation of the 5-OH-ip linker in **1a-1d**, we have selected two representative samples, **1c** and **1d**, both exhibiting high 5-OH-ip incorporation but quite different levels of Ru^{2+} and $Ru^{\delta+}$. As shown in Figure 4, upon CO_2 dosing for both the parent Ru-MOF and Ru-DEMOFs **1c**, an intense and broad IR band appears at 2336 cm^{-1} that is assigned to the asymmetric stretching mode $\nu_{as}(CO_2)$ of physisorbed CO_2 binding linearly at various Ru-sites.[15b] The weak band at 2273 cm^{-1} indicates the presence of a minority CO_2 species originating probably from the adsorption of a small amount of $^{13}CO_2$ with an expected isotopic shift of 1.03. Apart from the CO_2-related bands, two other bands at 2041 cm^{-1} and 1993 cm^{-1} have been observed in **1c**, that are assigned to vibrations of CO bound to the reduced $Ru^{\delta+}$-sites, matching our previous data on pydc-doped Ru-DEMOF.[20] This result indicates dissociative chemisorption of CO_2 to CO (reduction) in Ru-DEMOF with 5-OH-ip defect linker (**1c**), whereas the parent Ru-MOF is essentially inactive. However, in comparison to the extremely high reactivity of pydc-doped Ru-DEMOFs, in which CO_2 is nearly totally converted to CO at higher concentrations of pydc defective linker (e.g. 30%),[19] the production of CO is rather limited for 5-OH-ip doped Ru-DEMOFs (Figure 4). Interestingly, Ru-DEMOF **1d**, is almost inactive for CO_2 dissociation (Figure S19). We correlate this observation to the much less $Ru^{\delta+}$ and in turn to the more significant formation of missing node defects (type **B**) for **1d** as compared to **1c**. Overall, the presented IR data demonstrate that the 5-OH-ip doped Ru-DEMOF samples show much less reactivity for CO_2 activation as compared to pydc doped samples. This cannot be attributed only to the relatively low concentration of reduced $Ru^{\delta+}$. In our previous study,[19] we suggested the CO_2 activation being promoted by pydc linker due to the presence of basic pyridyl N sites in proximity to the reactive $Ru^{\delta+}$. This hypothesis is indirectly supported by the properties of samples **1c** and **1d.**

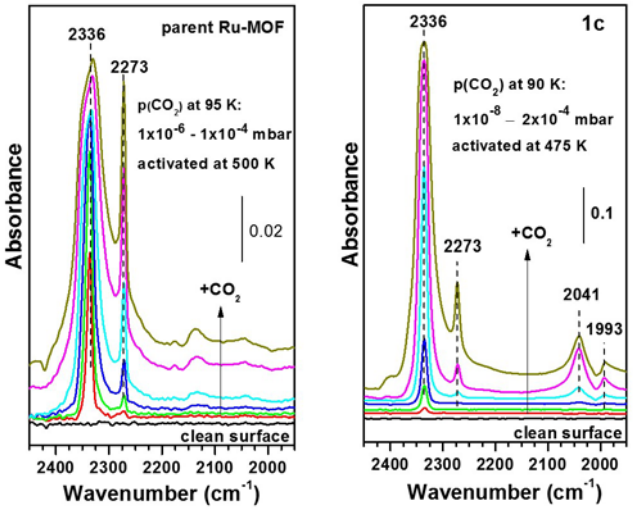

Figure 4. UHV-IR spectra of **1c** (right) compared with parent Ru-MOF (left) upon CO_2 dosing at 90-95 K after annealing the sample at 475-500 K. The bands at 2041 cm^{-1} and 1993 cm^{-1} are assigned to vibrations of CO bound to reduced $Ru^{\delta+}$-sites and indicate dissociative chemisorption of CO_2.

The combined spectroscopic characterization data (XANES, XPS, UHV-FTIR with CO and CO_2 as probes) presented above suggest more or less consistent, but complicated picture on the abundance of the two kinds of defects**.** Overall, we assume both types **A** and **B** being simultaneously generated in the Ru-DEMOFs in the case of coordinative weakly binding ligator-sites at the fragmented linkers. Type **A** appears to be favored at low incorporation levels, *e.g.* **1a** (8%) and becomes more abundant up to a certain threshold, *e.g.* **1c** (32%). Along with a further increase of incorporation level, *e.g.* **1d** (37%), defects of type **B** appear to dominate over type **A**. One should be aware that the possibility of formation and distribution of various defect types is rather diverse and may not be restrict to those mentioned here (see other possible defects and a summary of possible defect combinations in Table S8 and Figure S20, SI). Additional characterization and quantitative determination of the defect types requires additional work and support by theoretical modeling.

CO_2, CO and H_2 sorption properties of Ru-DEMOFs

The previous characterizations suggest the existence of two types of defects (**A** and **B**) being present in the samples in different absolute and relative amounts as a consequence of the 5-X-ip framework incorporation. Both are likely to influence the gas sorption properties of the Ru-DEMOFs. Hence, we studied the adsorption of CO_2, CO and H_2 at range of samples. In general, the results obtained and discussed in the following are not very conclusive as the observed changes in gas uptake as a function of defect linker incorporation are small or even close to the error of the measurements. Nevertheless, we present the data and provide a tentative discussion with respect to the possible counter acting effects of the two types of defects in the samples.

CO_2 adsorption isotherms (298 K) of the parent reference Ru-MOF sample and **1a** and **1c** display a gradual enhancement of the adsorption capacity in the order Ru-MOF < **1a** < **1c** along with rising incorporation degree of the defect linker (Figure S21). However, the CO_2 uptake of the sample **1d** revealed to be 2.9 mmol/g at 1 bar, and lies within the order Ru-MOF < **1d** < **1c** (Table S9). According to our studies on different defects in the series **1a-1d**, these results are not unexpected. The increase of the CO_2 uptake is attributed to the reduced Ru-sites at the type **A** defects and somewhat lowered uptake of **1d** is attributed to less abundant Ru-sites as a consequence of missing metal-nodes (*i.e.*, type **B** defects). Hence, higher incorporation level of the defect linker in the sample **1d** does not promote the increase of the CO_2 uptake.

Furthermore, CO adsorption of the parent Ru-MOF, **1a** and **1c** at 298 K also illustrates the tendency of enhanced uptake in case of the Ru-DEMOF samples (Figure S22). The small difference between the sample **1a** and the parent Ru-MOF on CO adsorption is attributed to the low incorporation degree of the 5-OH-ip defect linker (8%). Along with the increase of the defect linker incorporation (such as in **1c**), the CO uptake rises even at very low pressure (ca. 4 mbar). This increase of the CO capacity of the Ru-DEMOF is probably due to the generation of the modified paddlewheels of type **A**, which expose more open sites as one carboxylate ligator-site of btc is substituted by the hydroxyl-group of 5-OH-ip. Besides, the electronic density is varied as the oxidation state of ruthenium at the CUS is changed. Both could contribute to the enhancement of the adsorption properties.

The H_2 adsorption isotherms (at 77 K) of the parent Ru-MOF and the Ru-DEMOFs **1a** and **1c** follow nearly the same trend as in case of CO_2 and CO adsorption (Figure S23a). Both defect-engineered materials **1a** and **1c** exhibit higher H_2 uptake at 1 bar than the parent intact framework. However, H_2 capacity is slightly lower when the incorporation of 5-OH-ip is more than 8%, as in case of **1c** and **1d**. This could be due to the more significant generation of the type **B** defects in these Ru-DEMOFs. The calculated isosteric heats of adsorption ($-Q_{st}$) reveal an order with **1c** > **1a** > parent Ru-MOF when comparing the respective values at 1 mmol (H_2) / Ru_2-paddlewheel (what might be considered as the saturation adsorption of H_2 at the regular paddlewheel) (Figure S23b). This suggests stronger binding affinity of H_2 for Ru-DEMOF with 32% of incorporated 5-OH-ip (sample **1c**), which again is attributed to the relative higher amount of $Ru^{\delta+}$-sites in **1c**.

Moving further to the 5-NH_2-ip defect linker, respective Ru-DEMOFs (**3a-3c**) display the same tendencies in their absorption behavior of CO_2 and H_2 as in their S_{BET} (N_2). From the results of the XANES studies, we have already revealed that defects **B** are likely to be generated at lower doping levels **3a-c** (5-NH_2-ip) as compared to the samples **1a-d** (5-OH-ip). This difference in defect **A**/**B** abundance leads to variation of the CO_2 and H_2 adsorption in case of the **3a-c** series**.** Even though **3a-c** display higher uptake of CO_2 and H_2 than the parent Ru-MOF, the uptake of CO_2 and H_2 does not further increase after the feeding level of 5-NH_2-ip is raised above 10% (**3a**) (Figures S26 and S27). Similar to **1d,** we assign the decrease of the uptake of CO_2 and H_2 at 1 bar observed for **3c** as compared with **3a-b** to more abundant type **B** defects.

Another indication of the suggested counter acting effects of the defect sites is the comparison of the CO_2 and H_2 uptakes at **2a, 2b** and **4a** with the parent Ru-MOF (Figures S24, S25, S28 and S29). However, the variations are too small to be regarded as significant and will be not discussed here.

Catalytic test reactions

Ethylene dimerization utilizing MOF supported catalysts has recently attracted a lot of attention.[28] Most of the reported MOF catalysts bear isolated single-metal (*e.g.*, Ni, Ir) active-sites. Ru-MOF materials as heterogeneous catalysts for the ethylene dimerization have not been studied yet, although chemisorbed Ru-complex on de-aluminated zeolite Y and Ru-complex itself catalyzing ethylene to butene have been already reported.[29] It is known that the redox activity of Rh in RhCa-X Zeolite plays an important role on catalyzing ethylene dimerization.[30] Having distinct Ru-CUS available in the Ru-DEMOFs (*i.e.*, different Ru^{n+}-species being potentially involved into the redox-process(es) of the reaction flow), samples **1a** (8% of 5-OH-ip) and **1c** (32% of 5-OH-ip) have been selected for testing them as catalysts in the selected test reaction. In addition, parent Ru-MOF has been used as a reference. Thus, activated Ru-DEMOFs were loaded into a reactor to catalyze ethylene dimerization in toluene at different temperatures under the pressure of 800 psi (≈ 55 bar). In general, all reactions led to the formation of butene without producing any other α-olefins (Tables S10). Addition of Et_2AlCl as co-catalyst accelerates the conversion (Table S10, entry 2 *vs.* entry 3). When the reaction has been conducted at 26 °C, lower yield has been obtained compared to those at 80 °C (Table S10, entry 4 *vs.* entry 5). However, reactions conducted for 1 h and 24 h give almost the same TOF (0.88 *vs.* 0.92 h^{-1}), suggesting that the Ru-DEMOF **1c** does not suffer the deactivation as a function of on-stream time. Therefore, parent Ru-MOF and Ru-DEMOFs **1a** and **1c** have been employed to study the dimerization of ethylene in toluene under optimized condition (800 psi, 80 °C, 2 h) in the presence of Et_2AlCl. The obtained product was analyzed by gas chromatography. As we can see from entry 5-7 in Table S10 and Figure 5, the TOF value of **1a** and **1c** increase along with increase of the incorporation level of defect linker in comparison with the parent Ru-MOF. Since the contents of the reduced $Ru^{\delta+}$-sites in **1c** is the highest among the **1a-d** series (according to our study above), there should be more M-CUSs in **1c** and therefore it affords the chance to enhance the catalytic activity in the reaction. Indeed, the transformation of ethylene to butene is the highest (TOF = 4.36 h^{-1}) when employing **1c** as a catalyst. This value is still much lower than that using zeolite supported Ru-complex catalysts in the presence of H_2 (4.36 *vs.* 216 h^{-1}). However, it is higher than the TOF value (1 × 10-4 s^{-1} = 0.36 h^{-1}) in the reported reaction without the presence of H_2.[29b] Distinction between butene isomers, optimization of the reaction conditions using Ru-DEMOF materials (such as usage of H_2) as well as clarifying the mechanism of this reaction are currently under investigation. Nevertheless, the preliminary results give a rather clear hint that obtained Ru-materials could be utilized as catalyst for the dimerization of ethylene. Due to the diverse modification of MOF materials themselves, our current investigations on the ethylene dimerization using Ru-DEMOFs can afford a platform for further studies on MOFs as catalysts in this field.

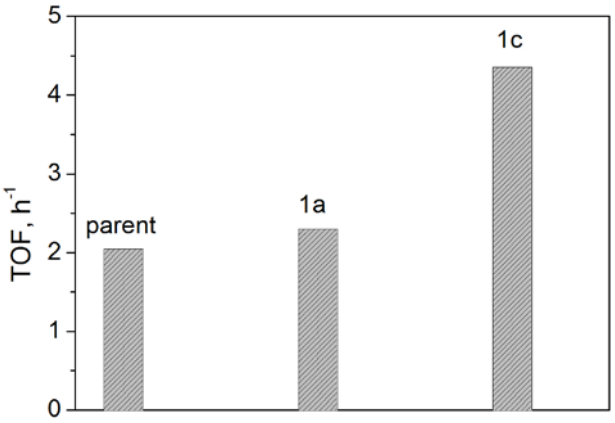

Figure 5. The tendency of TOF value for parent Ru-MOF and Ru-DEMOF samples **1a** and **1c** utilized as catalysts for transformation of ethylene into toluene (800 psi, 80 °C, 2h) in the presence of Et_2AlCl (0.81 ml, 1M in heptane). TOF (turnover frequency) = mol product / (mol Metal (catalyst)*h).

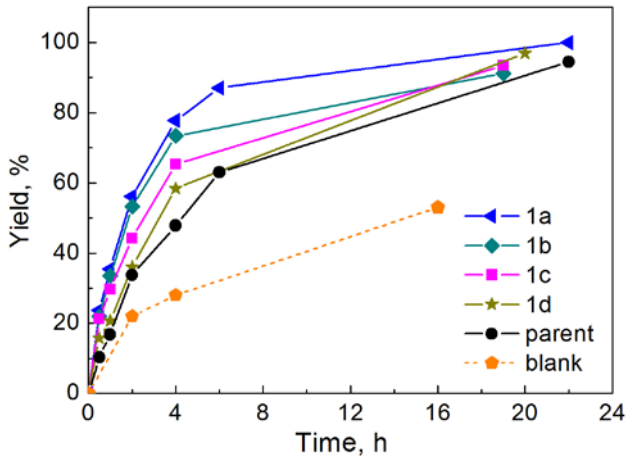

Figure 6. Time-yield plot of Paal-Knorr synthesis of phenylamine reacting with 2,5-hexadione, giving the pyrrole employing Ru-DEMOFs **1a**-**1d** (with 8%, 20%, 32% and 37% 5-OH-ip incorporation, respectively) as catalysts in comparison with the parent Ru-MOF(parent). Blank stands for the experiment where on catalyst was added into the reaction mixture.

Paal-Knorr pyrrole synthesis has attracted great attention due to the huge synthetic variety of pyrroles and their derivatives, which are key intermediates for various pharmaceutical drugs.[31] The reaction is typically performed under protic or Lewis acidic conditions, using primary amines and diketones. As we know from earlier reports, parent Ru-MOF ($[Ru_3(btc)_2Y_{1.5}]_n$) is constructed from Ru_2-paddlewheels, in which the axial Ru-positions are partly occupied by strongly binding Y or by other weakly guest molecules. After thermal treatment, a fraction of the axial positions can be exposed as open Lewis acidic sites (useful as catalytic site, for instance). With regard to the structure of the Ru-DEMOFs discussed in this contribution, two kinds of defects are present. The modified paddlewheel units (**A**) could provide the materials with additional sites around the partly reduced Ru-centers. On the other hand, the eliminated entire Ru-paddlewheel clusters (**B**) can form vacant-sites to play a role on affecting the adsorption properties, especially when the functional X-group at the defect generating linker is as small as H. Hence, Ru-DEMOFs **1a-1c**, **2a** and **2b** have been utilized for catalyzing the reaction of 2,5-hexadione and phenylamine in toluene at 90 °C to form dimethyl-phenyl-1*H*-pyrrole (Scheme 1).

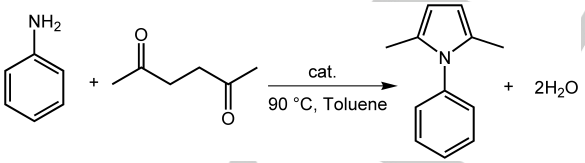

Scheme 1. The Paal-Knorr catalytic reaction.

It is interesting to note that all of the selected Ru-DEMOFs show apparently enhanced conversion of phenylamine to the pyrrole within the initial 4 hours in comparison with the parent Ru-MOF (Figure 6). All the samples tested were found to be stable under reaction conditions, as confirmed by comparing the PXRD of fresh and used materials.

Among the used materials, Ru-DEMOFs **1a** and **2a** exhibit the highest catalytic activity, although the other Ru-DEMOFs (**1b, 1c, 1d** and **2b**) incorporate more defect linker (Table S11). The steric hindrances and distinct defect types (**A** *vs.* **B**) could be the main reason of this phenomenon. When Ru-DEMOF samples with 5-OH-ip defect linker (**1a-d**) were employed as catalysts, the yield of pyrrole has been increased from 48% (using parent Ru-MOF as the catalyst) to 58% (**1d**), 65% (**1c**), 73% (**1b**) and 77% (**1a**), respectively. This is assigned to the presence of the reduced Ru-centers (defects of type **A**) in these materials. Reduced, softer binding $Ru^{\delta+}$-sites can be more easily coordinated to the O atom of the carbonyl group, which favors the nucleophilic attack from the lone-pair of the amino group of phenylamine. However, when the incorporation of 5-OH-ip increases, the gradual dominance of the defects **B** in these materials probably eliminates part of the reactive metal centers, thus, affecting the catalytic activity of the **1b-d** samples. On the other hand, Ru-DEMOF **2a** displays higher yield of pyrrole compared to the parent Ru-MOF (82% *vs.* 48%), regardless of the partial absence of the metal centers (defects **B**) (Figure S30). This could be a result of the smaller steric hindrance surrounding the Ru-CUSs while employing the H_2ip defect linker. When the contents of the incorporated defect linkers are rather small (*i.e.*, as in **2a**), the negative influence caused by missing metal centers is relatively insignificant compared with the positive effect of the smaller steric hindrance. Therefore, **2a** Ru-MOF material shows as high catalytic activity in present reaction as **1a**. Similar observations have been found for the samples **1b-c** because of the somewhat larger steric hindrance of OH-groups in spite of the type **A** defect in these materials.

Conclusions

Applying the solid solution approach, a range of Ru-DEMOFs ($[Ru_3(btc)_{2-x}(5\text{-X-ip})_xY_y]_n$) isostructural to HKUST-1 were obtained with the framework incorporated defect linkers 5-OH-ip (**1a-d**), ip (**2a** and **2b**), 5-NH_2-ip (**3a-c**) and 5-Br-ip (**4a**)). Comparably high S_{BET} have been measured for Ru-DEMOF samples (947-1302

m^2/g) when considering the parent Ru-MOF material $[Ru_3(btc)_2Y_{1.5}]_n$ (704-998 m^2/g).[15a, 23] The highest level of defect linker incorporation appeared to be 37% (**1d,** 5-OH-ip). The data are consistent with two kinds of defects (**A** and **B**) being introduced to the Ru-DEMOFs depending on the nature of the functional groups (X) of the defect linkers (5-X-ip; see Figure 1). Defect linkers with steric less demanding X-groups of probably still existing, but weaker coordinative binding properties as a carboxylate ligator are likely to favor type **A** defects, defined as modified paddlewheel nodes exhibiting reduced $Ru^{\delta+}$-sites. Along with the increasing of the defect linker contents, defects of type **B**, *i.e.* missing node defects, can be created simultaneously in the DEMOFs. When the functional groups in the defect linker 5-X-ip are much smaller than carboxylate and non-coordinating X (such as H), the defects of type **B**, defined as missing node defects, apparently become more dominant even in case of low doping level (case of **2a** and **2b**). The more or less simultaneous presence of two kinds of defects leads to the synergetic and as well counteracting effects on the porosity, sorption and catalytic properties. In fact, Ru-DEMOF **1c** (32% 5-OH-ip incorporation), in which defects of type **A** are more dominant, reveals the highest BET surface area (1302 m^2/g) among the all samples, including parent Ru-MOF and its DEMOF derivatives reported so far.[20] Concerning the enhanced gas sorption properties, type **A** defects are more important than those effects related to the defects of type **B**, as reduced and more accessible $Ru^{\delta+}$-sites have been produced in defect type **A**. When it comes to the catalytic activity, $Ru^{\delta+}$-sites in Ru-DEMOF **1c** are suggested to be responsible for the significant increase of TOF value of ethylene dimerization, as clearly seen while comparing with the parent Ru-MOF and **1a,** in which no or less $Ru^{\delta+}$-sites are present. However, in case of Paal-Knorr pyrrole reaction, the possible steric hindrance between the functional groups (OH) at the defect linker and 2,5-hexadione substrate is suggested to be responsible for the reduced activity of the Ru-DEMOFs **1a-d**, although they all feature enhanced conversion compared with the parent Ru-MOF. All in all, the described Ru-DEMOFs obtained *via* solid solution approach employing various defect linkers turned out to be rather complex materials to be studied and characterized. Nevertheless, the observed spectroscopic evidences as well as effects on sorption properties and catalytic performance reasonably fit into a model of the two types of defects, modified and missing nodes (see Figure 1), respectively.

Experimental Section

Materials. Ruthenium SBU precursor $[Ru_2(OOCCH_3)_4Cl]_n$[32] as well as the parent single-linker Ru-MOF[15] were prepared following procedures previously described in the literature. All other reagents were available commercially and used without further purification. Before further manipulations, all activated samples were stored in a glove-box under inert Ar atmosphere.

Methods. The Powder X-Ray diffraction (PXRD) data for all the as-synthesized samples and activated samples (**2a**-**2d**, **4a**-**4c**) were performed on an X' Pert PRO PANalytical equipment (Bragg–Brentano geometry with automatical divergence slits, position sensitive detector, continuous mode, room temperature, Cu-Kα radiation, Ni-filter, in the range of 2θ = 5–50°, step size 0.01°). Activated sample were prepared on a silicon wafer in an Ar-filled glovebox right before the measurement starts. For the measurement of activated samples (Ru-DEMOFs series **1** and **3**), the data were collected at beam line BL9 of the synchrotron radiation facility DELTA at a wavelength of 0.4592 Å using a two-dimensional MAR345 image plate detector. The sample was filled into standard capillaries (0.5-mm diameter) in an Ar-filled glovebox and measured. The data were integrated using the program package Fit2D[33] and transformed to the CuKα radiation (λ = 1.54178 Å) used for all other PXRD measurements on reported materials for the convenient comparison. Elemental Analyses data were obtained from the Mikroanalytisches Laboratorium Kolbe in Mülheim an der Ruhr (http://www.mikro-lab.de/index.html). Samples were filled into finger Schlenks in an Ar-filled glovebox and measured under Ar. FTIR spectra were collected on a Bruker Alpha FTIR instrument in the ATR geometry with a diamond ATR unit in the range 400–4000 cm^{-1} inside a LABStar MB 10 compact MBraun glove-box (argon atmosphere). (TEM-)EDX spectra for the composition determination of sample **4a-4c** were recorded on a Tecnai G^2 F20 equipped with a Schottky field emission gun operated at an acceleration voltage of 200 kV at the department of Mechanical Engineering, Ruhr-University Bochum. Liquid phase ^{1}H-NMR spectra were measured on a Bruker Avance DPX-200 spectrometer at 293 K in DCl/DMSO-d_6 for the digested activated MOF samples. CO adsorption (298 K) and the majority of N_2 (99.999%) sorption (77 K) measurements were performed using a Micromeritics 3Flex instrument. The N_2 sorption isotherms of **3a-3d** were collected using a Quantachrome Autosorp-1 MP instrument, optimized protocols and N_2 of 99.9995% purity. Experiments on sorption of CO_2 (298 K) and H_2 (77 K) were conducted on a Micromeritics ASAP 2020 gas adsorption analyzer. The thermogravimetric analyses (TGA) were collected using a TG/DSC NETZSCH STA 409 PC instrument at a heating rate of 5 K min^{-1} in a temperature range from 30–600 °C at atmospheric pressure (sample weight 5–10 mg, N_2 (99.999%;) gas flow (20 ml min^{-1}). XANES spectra were recorded at the Ru-*K* edge (22117 eV) using a Si (311) monochromator at Beamline BL8 of the synchrotron radiation facility DELTA, TU Dortmund. The samples were filled into 1 mm caplillaries in an inert Ar atmosphere glovebox before the measurement. The XANES measurements were acquired using 15cm Ionchamber filled with Ar as I0, a 15 cm Ionchamber filled with Xe as I1 and a 30 cm Ionchamber filled with Xe as I2. Approx 30 mm above the sample was the PIN-Diode capturing a relatively wide solid angle of fluorescence radiation. The energy was calibrated by measuring a metallic Ru foil as reference simultaneously to each sample scan. The data processing and analysis were done using the program ATHENA.[34] Ultra High Vacuum (UHV) FT-IR measurements were performed using a novel UHV-FTIRS apparatus. The powder samples were first pressed into a stainless steel grid covered by gold and then mounted on a sample holder, which was specially designed for the FTIR transmission measurements under UHV conditions. The grid was cleaned by heating up to 850 K to remove all contaminants formed on it during preparation. The base pressure in the measurement chamber was 5 x 10^{-11} mbar. The optical path inside the IR spectrometer and the space between the spectrometer and UHV chamber were also evacuated to avoid atmospheric moisture adsorption resulting in a high sensitivity and stability. The MOF samples were cleaned in the UHV chamber by heating to 500 K in order to remove the contaminants involved during synthesis and all the adsorbed species such as water and hydroxyl groups. Prior to each exposure, a spectrum of the clean sample was recorded to be as a background reference. The exposure of the sample to CO and CO_2 was carried out by backfilling the measurement chamber through a leak valve. All UHV-FTIR spectra were collected with 512 scans at a resolution of 4 cm^{-1} in transmission mode. X-ray photoelectron spectroscopy (XPS) measurements were performed in a UHV setup equipped with a high-resolution Gammadata-Scienta SES 2002 analyzer. A monochromatic Al Kα X-ray source (energy 1486.6 eV) was used as incident radiation. The analyzer slit width was set at 0.3 mm and the pass energy was fixed at 200 eV for all the measurements. The overall energy resolution was better than 0.5 eV. A flood gun was used to compensate for the charging effects. All spectra reported here are calibrated to the C 1s corelevel binding energy at 285 eV. The XP spectra were deconvoluted using the CASA XPS program with a mixed Gaussian−Lorentzian function and Shirley background

subtraction. Gas Chromatography measurements for Paal-Knorr reaction were performed on an Agilent Technologies 7890A with FID (Flame Ionization Detector) using a capillary column HP-5 (5% phenylmethylpolysiloxane) of 30 m length and 0.32 mm internal diameter as well as BP20(WAX) of 15 m length and 0.32 mm internal diameter as another column. Thereby, the samples were measured in high dilution using volatile organic solvents (usually ethanol or acetone).

Synthesis of Ru-DEMOF samples (1a-1d, 2a-2d, 3a-3d, 4a-4c)

$[Ru_3(btc)_{2-x}(5\text{-X-ip})_xY_y]_n$ (Y = counter ion; 0.1 ≤ x ≤ 1; 0 ≤ y ≤ 1.5). The samples were synthesized according to the reported method[20] applying the so-called controlled SBU approach. The mixtures of parent linker (1,3,5-benzenetricarboxylic acid, *i.e.* H_3btc) and defective linker (5-X-isophthalic acid, *i.e.* 5-X-ipH_2, X = OH (**1**), H (**2**), NH_2 (**3**) and Br (**4**), respectively) combined with 1.5 molar equivalents of $[Ru_2(OOCCH_3)_4Cl]_n$ (0.36 mmol,170 mg) were placed in the 20 ml Teflon vessels. Subsequently, 4 ml of HPLC grade water and 0.7 ml of glacial acetic acid were added. The molar ratios and amounts of the linkers used in the starting materials are listed in the Table S1**.** The Teflon reaction vessels were then placed in the Teflon-lined stainless steel autoclaves. The autoclaves were further sealed and placed into the pre-heated oven at 433 K for 72 h. Afterwards the autoclaves were taken out and cooled down at room temperature. The resulting powder products were collected by centrifugation. Afterwards, they were soaked into HPLC grade water (ca. 20 ml) and the solvent was refreshed by the same water amount every 24 hours for 3 times. Finally, the solvent was removed and collected powders were dried under air at room temperature. The activation of the solids was performed by heating at 423 K for 24 h under dynamic vacuum (ca. 10^{-3} mbar).

Catalytic reactions

1. Ethylene dimerization

In a typical run (entry 5), 2.1 mg of the activated Ru-MOF **1c** was put in a 10 ml steel reactor followed by adding of 0.81 ml of Et_2AlCl (1M in heptane), 2.1 ml of toluene and 0.09 ml of undecane (0.01 M in toluene). After degassing, the reactor was flushed with C_2H_4 (800psi) and placed in a pre-heated oil bath at 80 °C with stirring for 2 hours. Subsequently, the reaction was stopped and the reactor was cooled down at -7 °C in a mixture of dry ice and ethylene glycol bath. Cold distilled water was added to quench the reaction. The organic layer kept cold was then quickly analyzed by gas chromatography (SRI 8610V GC, 60 m x 0.54 mm internal diameter, 5.0 µm MXT-1 capillary columns) using undecane signal as a reference. For other entries, the amount of catalysts, the reaction temperature and time were varied and listed in Table S10. In case of no additive, the volume of toluene was changed to 2.91 ml. Other parameters are the same as entry 5 described above.

2. Paal-Knorr reaction

In a typical run, 5 mg of the activated Ru-MOF/DEMOFs in 0.5 ml of toluene were introduced into 125 mg (1.1 mmol) of 2,5-hexadione and 95 mg (1 mmol) of phenylamine and were stirred at 90 °C for 24h under air. The reaction was followed by taking aliquots every hour and analyzing the products by GC-MS. The reactions were performed in closed (pressurized) reaction vials.

Acknowledgements

This research was partially supported by the DFG project FI-502/32-1. W.Z. thanks for a PhD fellowship from the China Scholarship Council (CSC). W.Z is also grateful to the Research School^{Plus} at Ruhr-University Bochum for the support of her PhD project and funding of an internship at UC Berkeley at the group of Prof. J. R. Long and collaboration with D.J.X and M.G including Douglas Reed for the collection of CO isotherms (298K). W.Z. also thanks Dr. Raghavender Medishetty for the fruitful discussions. P.G. acknowledges the support of the EU innovative Training Network "DEFect NETwork materials science and engineering" (DEFNET). The authors further thank the team at DELTA synchrotron facility at the TU Dortmund for the support with the X-ray absorption spectroscopy experiments performed at beam lines BL8 and the PXRD data collection at beam lines BL9.

Keywords: metal-organic frameworks • structural defects • ruthenium • sorption • heterogeneous catalysis

[1] a) M. Latroche, S. Surblé, C. Serre, C. Mellot-Draznieks, P. L. Llewellyn, J.-H. Lee, J.-S. Chang, S. H. Jhung, G. Férey, *Angew. Chem. Int. Ed.* **2006**, *45*, 8227-8231; b) X. Lin, J. Jia, X. Zhao, K. M. Thomas, A. J. Blake, G. S. Walker, N. R. Champness, P. Hubberstey, M. Schröder, *Angew. Chem. Int. Ed.* **2006**, *45*, 7358-7364; c) K. Sumida, D. L. Rogow, J. A. Mason, T. M. McDonald, E. D. Bloch, Z. R. Herm, T.-H. Bae, J. R. Long, *Chem. Rev.* **2012**, *112*, 724-781.

[2] a) A. Schneemann, E. D. Bloch, S. Henke, P. L. Llewellyn, J. R. Long, R. A. Fischer, *Chem. Eur. J.* **2015**, *21*, 18764-18769; b) E. D. Bloch, M. R. Hudson, J. A. Mason, S. Chavan, V. Crocellà, J. D. Howe, K. Lee, A. L. Dzubak, W. L. Queen, J. M. Zadrozny, S. J. Geier, L.-C. Lin, L. Gagliardi, B. Smit, J. B. Neaton, S. Bordiga, C. M. Brown, J. R. Long, *J. Am. Chem. Soc.* **2014**, *136*, 10752-10761; c) E. D. Bloch, W. L. Queen, R. Krishna, J. M. Zadrozny, C. M. Brown, J. R. Long, *Science* **2012**, *335*, 1606-1610; d) T. Rodenas, I. Luz, G. Prieto, B. Seoane, H. Miro, A. Corma, F. Kapteijn, F. X. Llabrés i Xamena, J. Gascon, *Nat. Mater.* **2015**, *14*, 48-55.

[3] a) J. S. Seo, D. Whang, H. Lee, S. I. Jun, J. Oh, Y. J. Jeon, K. Kim, *Nature* **2000**, *404*, 982-986; b) A. Corma, H. García, F. X. Llabrés i Xamena, *Chem. Rev.* **2010**, *110*, 4606-4655.

[4] E. Biemmi, C. Scherb, T. Bein, *J. Am. Chem. Soc.* **2007**, *129*, 8054-8055.

[5] P. Horcajada, C. Serre, M. Vallet-Regí, M. Sebban, F. Taulelle, G. Férey, *Angew. Chem. Int. Ed.* **2006**, *45*, 5974-5978.

[6] a) R. A. Beyerlein, C. Choi-Feng, J. B. Hall, B. J. Huggins, G. J. Ray, *Top. Catal.*, *4*, 27-42; b) C. Baerlocher, D. Xie, L. B. McCusker, S.-J. Hwang, I. Y. Chan, K. Ong, A. W. Burton, S. I. Zones, *Nat. Mater.* **2008**, *7*, 631-635; c) B. Bonelli, L. Forni, A. Aloise, J. B. Nagy, G. Fornasari, E. Garrone, A. Gedeon, G. Giordano, F. Trifirò, *Micropor. Mesopor. Mat.* **2007**, *101*, 153-160.

[7] Z. Fang, B. Bueken, D. E. De Vos, R. A. Fischer, *Angew. Chem. Int. Ed.* **2015**, *54*, 7234-7254.

[8] U. Ravon, M. Savonnet, S. Aguado, M. E. Domine, E. Janneau, D. Farrusseng, *Micropor. Mesopor. Mat.* **2010**, *129*, 319-329.

[9] F. Vermoortele, B. Bueken, G. Le Bars, B. Van de Voorde, M. Vandichel, K. Houthoofd, A. Vimont, M. Daturi, M. Waroquier, V. Van Speybroeck, C. Kirschhock, D. E. De Vos, *J. Am. Chem. Soc.* **2013**, *135*, 11465-11468.

[10] F. G. Cirujano, A. Corma, F. X. Llabrés i Xamena, *Chem. Eng. Sci.* **2015**, *124*, 52-60.

[11] S. S. Y. Chui, S. M. F. Lo, J. P. H. Charmant, A. G. Orpen, I. D. Williams, *Science* **1999**, *283*, 1148-1150.

[12] a) M. Kramer, U. Schwarz, S. Kaskel, *J. Mater. Chem.* **2006**, *16*, 2245-2248; b) C. R. Wade, M. Dinca, *Dalton Trans.* **2012**, *41*, 7931-7938.

[13] L. J. Murray, M. Dinca, J. Yano, S. Chavan, S. Bordiga, C. M. Brown, J. R. Long, *J. Am. Chem. Soc.* **2010**, *132*, 7856-7857.

[14] P. Maniam, N. Stock, *Inorg. Chem.* **2011**, *50*, 5085-5097.

[15] a) O. Kozachuk, K. Yusenko, H. Noei, Y. Wang, S. Walleck, T. Glaser, R. A. Fischer, *Chem. Commun.* **2011**, *47*, 8509-8511; b) H. Noei, O. Kozachuk, S. Amirjalayer, S. Bureekaew, M. Kauer, R. Schmid, B. Marler, M. Muhler, R. A. Fischer, Y. Wang, *J. Phys. Chem. C* **2013**, *117*, 5658-5666.

[16] J. I. Feldblyum, M. Liu, D. W. Gidley, A. J. Matzger, *J. Am. Chem. Soc.* **2011**, *133*, 18257-18263.

[17] S. Marx, W. Kleist, A. Baiker, *J. Catal.* **2011**, *281*, 76-87.

[18] Z. Fang, J. P. Dürholt, M. Kauer, W. Zhang, C. Lochenie, B. Jee, B. Albada, N. Metzler-Nolte, A. Pöppl, B. Weber, M. Muhler, Y. Wang, R. Schmid, R. A. Fischer, *J. Am. Chem. Soc.* **2014**, *136*, 9627-9636.

[19] G. Barin, V. Krungleviciute, O. Gutov, J. T. Hupp, T. Yildirim, O. K. Farha, *Inorg. Chem.* **2014**, *53*, 6914-6919.

[20] O. Kozachuk, I. Luz, F. X. Llabrés i Xamena, H. Noei, M. Kauer, H. B. Albada, E. D. Bloch, B. Marler, Y. Wang, M. Muhler, R. A. Fischer, *Angew. Chem. Int. Ed.* **2014**, *53*, 7058-7062.

[21] F. Schröder, D. Esken, M. Cokoja, M. W. E. van den Berg, O. I. Lebedev, G. Van Tendeloo, B. Walaszek, G. Buntkowsky, H.-H. Limbach, B. Chaudret, R. A. Fischer, *J. Am. Chem. Soc.* **2008**, *130*, 6119-6130.

[22] E. A. Braude, F. C. Nachod, Editors, *Determination of Organic Structures by Physical Methods*, Academic Press, **1955**.

[23] W. Zhang, O. Kozachuk, R. Medishetty, A. Schneemann, R. Wagner, K. Khaletskaya, K. Epp, R. A. Fischer, *Eur. J. Inorg. Chem.* **2015**, *2015*, 3913-3920.

[24] F. Genin, F. Quiles, A. Burneau, *Phys. Chem. Chem. Phys.* **2001**, *3*, 932-942.

[25] K. Nakamoto, in *Infrared and Raman Spectra of Inorganic and Coordination Compounds*, John Wiley & Sons, Inc., **2008**, pp. 1-273.

[26] Z. Wang, J. Liu, B. Lukose, Z. Gu, P. G. Weidler, H. Gliemann, T. Heine, C. Wöll, *Nano Letters* **2014**, *14*, 1526-1529.

[27] K. S. W. Sing, D. H. Everett, R. A. W. Haul, L. Moscou, R. A. Pierotti, J. Rouquerol, T. Siemieniewska, *Pure Appl. Chem.* **1985**, *57*, 603-619.

[28] a) S. T. Madrahimov, J. R. Gallagher, G. Zhang, Z. Meinhart, S. J. Garibay, M. Delferro, J. T. Miller, O. K. Farha, J. T. Hupp, S. T. Nguyen, *ACS catal.* **2015**, *5*, 6713-6718; b) D. Yang, S. O. Odoh, J. Borycz, T. C. Wang, O. K. Farha, J. T. Hupp, C. J. Cramer, L. Gagliardi, B. C. Gates, *ACS catal.* **2016**, *6*, 235-247; c) J. Canivet, S. Aguado, Y. Schuurman, D. Farrusseng, *J. Am. Chem. Soc.* **2013**, *135*, 4195-4198; d) E. D. Metzger, C. K. Brozek, R. J. Comito, M. Dincă, *ACS Cent. Sci.* **2016**.

[29] a) I. Ogino, B. C. Gates, *Chem. Eur. J.* **2009**, *15*, 6827-6837; b) I. Ogino, B. C. Gates, *J. Am. Chem. Soc.* **2008**, *130*, 13338-13346; c) G. Laurenczy, A. E. Merbach, *J. Chem. Soc., Chem. Commun.* **1993**, 187-189.

[30] J. S. Bass, L. Kevan, *J. Phys. Chem.* **1990**, *94*, 1483-1489.

[31] a) A. L. Harreus, in *Ullmann's Encyclopedia of Industrial Chemistry*, Wiley-VCH Verlag GmbH & Co. KGaA, **2000**; b) R. J. Sundberg, in *Comprehensive Heterocyclic Chemistry II* (Ed.: Scriven), Pergamon, Oxford, **1996**, pp. 119-206.

[32] R. W. Mitchell, A. Spencer, G. Wilkinson, *J. Chem. Soc., Dalton Trans.* **1973**, 846-854.

[33] A. P. Hammersley, S. O. Svensson, M. Hanfland, A. N. Fitch, D. Hausermann, *High Pressure Res.* **1996**, *14*, 235-248.

[34] B. Ravel, M. Newville, *J. Synchrotron Radiat.* **2005**, *12*, 537-541.

Entry for the Table of Contents (Please choose one layout)

Layout 1:

FULL PAPER

Employing mixed component solid solution approach, various 5-X-isophthalate linkers have been introduced into the Ru-analogue of HKUST-1 to yield the isoreticular, defect-engineered Ru-MOFs. The characterization data are consistent with two kinds of **defects** (**type A**: modified paddlewheels and **type B**: missing paddlewheels) and their relative abundance is controlled by nature of the functional X-group of the defect generating linkers. Porosity, sorption and reactive properties correlate with the proposed defect structure.

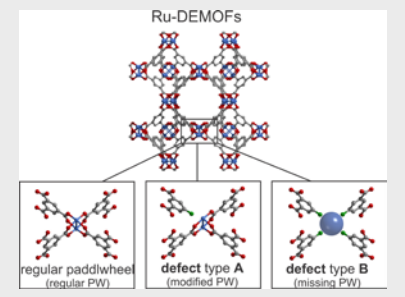

Key Topic*

metal-organic frameworks • structural defects

Wenhua Zhang, Max Kauer, Olesia Halbherr, Konstantin Epp, Penghu Guo, Miguel Gonzalez, Dianne J. Xiao, Christian Wiktor, Francesc X. LIabrés i Xamena, Christof Wöll, Yuemin Wang, Martin Muhler, and Roland A. Fischer**

Page No. – Page No.

Ruthenium Metal-Organic Frameworks with Different Defect Types: Influence on Porosity, Sorption and Catalytic Properties

Ruthenium Metal-Organic Frameworks with Different Defect Types: Influence on Porosity, Sorption and Catalytic Properties

Wenhua Zhang,[a] Max Kauer,[a] Olesia Halbherr,[a] Konstantin Epp,[b] Penghu Guo,[c] Miguel Gonzalez,[d] Dianne J. Xiao,[d] Christian Wiktor,[a] Francesc X. LIabrés i Xamena,[e] Christof Wöll,[f] Yuemin Wang,[f]* Martin Muhler,[c] and Roland A. Fischer*[b]

[a] W. Zhang, Dr. O. Halbherr, M. Kauer, Dr. C. Wiktor
Chair of Inorganic Chemistry II
Ruhr-University Bochum,
Universitätsstrasse 150, 44801 Bochum (Germany)

[b] K. Epp, Prof. Dr. R. A. Fischer
Chair of Inorganic and Metal-Organic Chemistry
Technical University Munich,
Lichtenbergstraße 4, D-85748 Garching (Germany)
E-mail: roland.fischer@tum.de

[c] P. Guo, Prof. Dr. M. Muhler
Laboratory of Industrial Chemistry
Ruhr-University Bochum (Germany)
Universitätsstrasse 150, 44801 Bochum (Germany)

[d] M. Gonzalez, D. J. Xiao
Department of Chemistry
University of California, Berkeley
Berkeley 94720 California (USA)

[e] Dr. F. X. LIabrés i Xamena
Instituto deTecnología Química (ITQ)
Universitat Politècnica de València
Consejo Superior de Investigaciones Científicas
Avenida de los Naranjos s/n, 46022 Valencia (Spain)

[f] Prof. Dr. Ch. Wöll, Dr. Y. Wang
Institute of Functional Interfaces (IFG)
Karlsruhe Institute of Technology (KIT), Karlsruhe (Germany)
E-mail: yuemin.wang@kit.edu

Table of Contents

1. Experimental information

Table S1. Feeding molar ratios and amounts of the linkers used in the syntheses of the **Ru-DEMOF samples.**

Sample	parent linker (H_3btc)		defect linker (5-X-ipH_2)		
	molar ratio of H_3btc : (H_3btc + 5-X-ipH_2)	mass (mg)		molar ratio of 5-X-ipH_2 : (H_3btc + 5-X-ipH_2)	mass (mg)
1a	90%	90.8	X = OH	10%	9
1b	80%	80.7		20%	18
1c	70%	71		30%	26
1d	50%	50.5		50%	43.7
2a	90%	90.8	X = H	10%	8
2b	80%	80.7		20%	16
2c	70%	71		30%	24
2d	50%	50.5		50%	40
3a	90%	90.8	X = NH_2	10%	8.7
3b	80%	80.7		20%	17.4
3c	70%	71		30%	26
3d	50%	50.5		50%	43.5
4a	90%	90.8	X = Br	10%	12
4b	80%	80.7		20%	24
4c	70%	71		30%	35.3

2. PXRD analysis

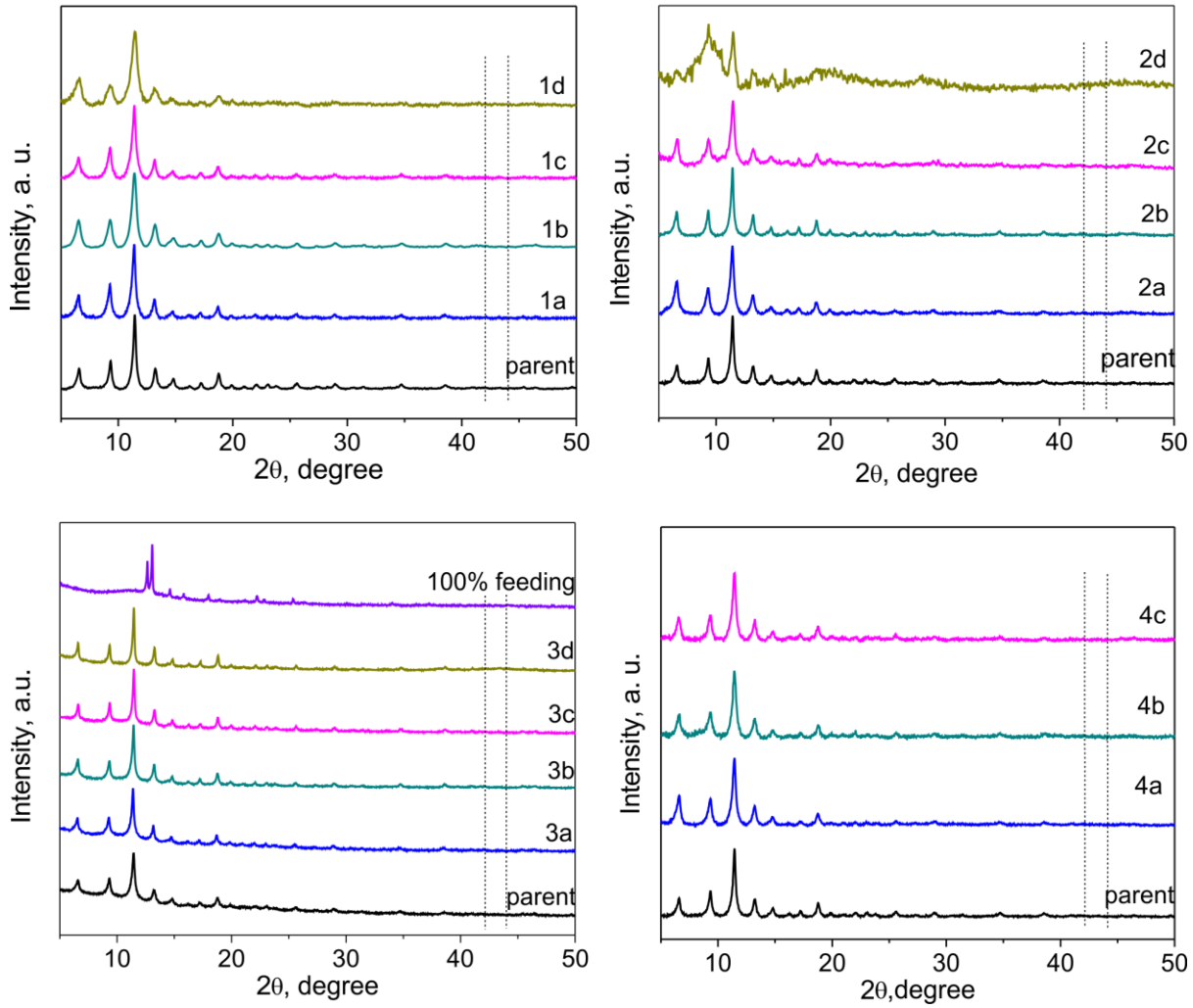

Figure S1. PXRD patterns of the solvated Ru-DEMOF materials **1a-1d, 2a-2d, 3a-3d, 4a-4c** compared with the solvated parent Ru-MOF, respectively. **1a-1d**: defect linker is 5-OH-ip; from **1a** to **1d**, feeding level is increasing: 10%, 20%, 30%, 50%, respectively. **2a-2d**: defect linker is ip; from **2a-2d**, feeding level is increasing: 10%, 20%, 30%, 50%, respectively. **3a-3d**: defect linker is 5-NH_2-ip, from **3a** to **3d**, feeding level is increasing: 10%, 20%, 30%, 50%, respectively. **4a-4c**: defect linker is 5-Br-ip, from **4a** to **4c**, the feeding level is increasing: 10%, 20%, 30%, respectively. Vertical lines at 42.1° and 44° stand for the respective reflections of (001) and (101) faces of hexagonal close-packed metallic Ru-particles or Ru-NPs.

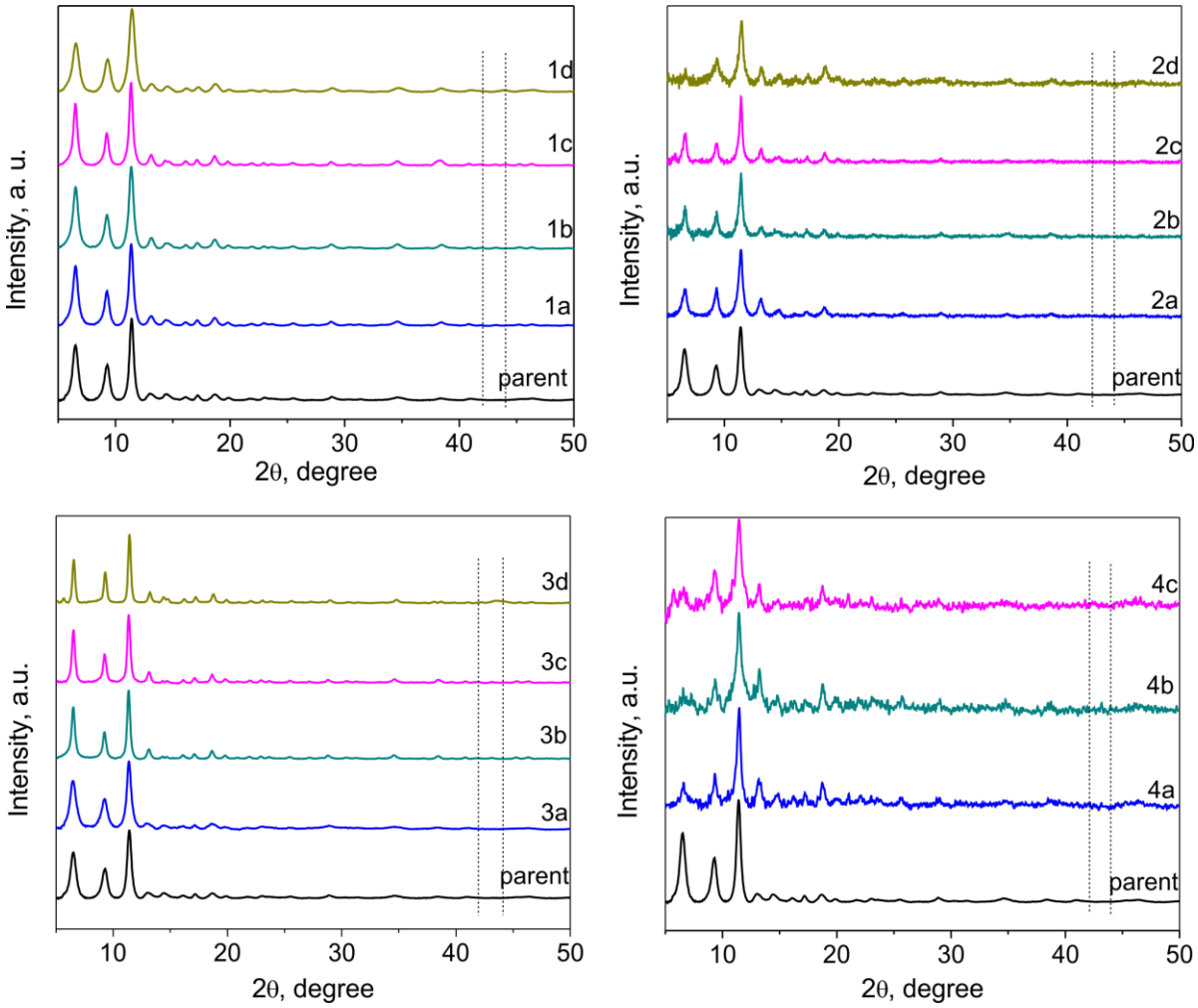

Figure S2 PXRD patterns of the activated Ru-DEMOF materials **1a-1d, 2a-2d, 3a-3d, 4a-4c** compared with the solvated parent Ru-MOF, respectively. **1a-1d**: defect linker is 5-OH-ip; from **1a** to **1d**, feeding level is increasing: 10%, 20%, 30%, 50%, respectively. **2a-2d**: defect linker is ip; from **2a-2d**, feeding level is increasing: 10%, 20%, 30%, 50%, respectively. **3a-3d**: defect linker is 5-NH_2-ip, from **3a** to **3d**, feeding level is increasing: 10%, 20%, 30%, 50%, respectively. **4a-4c**: defect linker is 5-Br-ip, from **4a** to **4c**, the feeding level is increasing: 10%, 20%, 30%, respectively. Vertical lines at 42.1° and 44° stand for the respective reflections of (001) and (101) faces of hexagonal close-packed metallic Ru-particles or Ru-NPs.

3. TGA

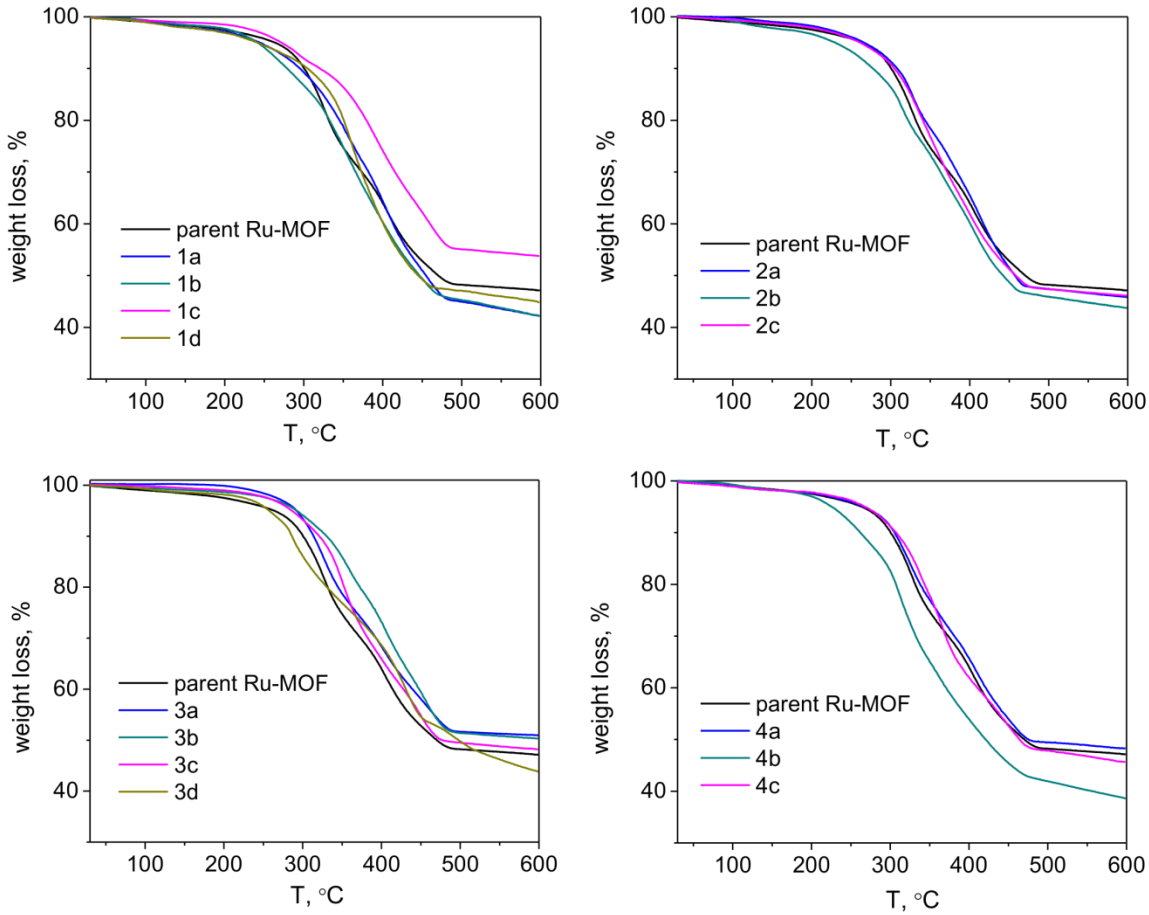

Figure S3. TG curves of the prepared Ru-DEMOFs **1a-1d** (with 5-OH-ip defect linker)**, 2a-2c** (with ip defect linker)**, 3a-3d** (with 5-NH_2-ip defect linker), **4a-4c** (with 5-Br-ip defect linker) in comparison with the parent Ru-MOF, respectively.

4. ^{1}H-NMR spectroscopic analysis

Table S2. The molar percentages of the defect linkers used for the synthesis and observed in the final Ru-DEMOFs in respect to the total amount of linkers (H_3btc + 5-X-ipH_2 = 100%). For the samples **1a-1d** defect linker is 5-OH-ip; for **2a-2c** – ip; for **4a-4c** – 5-Br-ip, respectively.

Sample	Feeding (used for synthesis)	Obtained
1a	10%	8%
1b	20%	20%
1c	30%	32%
1d	50%	37%
2a	10%	15%

2b	20%	28%
2c	30%	47%
4a	10%	17%
4b	20%	25%
4c	30%	42%

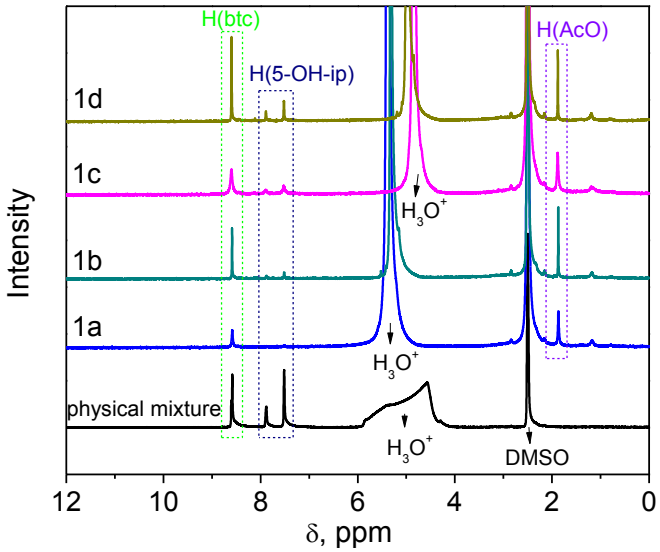

Figure S4. ^{1}H-NMR spectra of the Ru-DEMOFs (**1a-1d)** digested in DCl/DMSO-d_6 mixture. Defect linker is 5-OH-ip. H_3O^+ comes from H_2O and HCl contained in DCl.

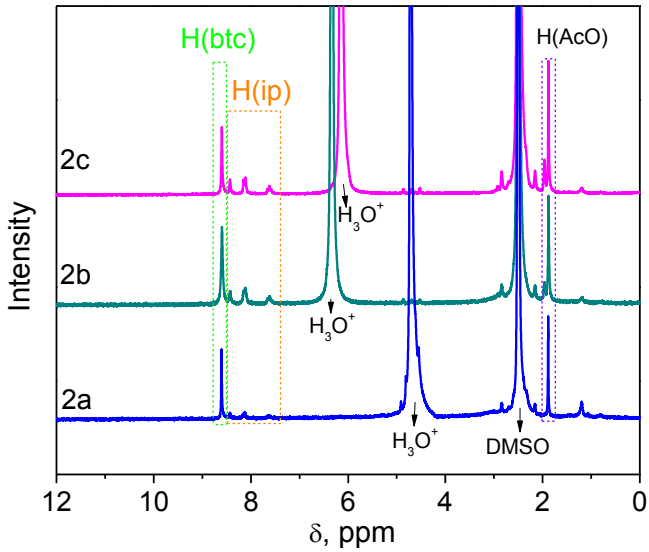

Figure S5. ^{1}H-NMR spectra of the Ru-DEMOFs (**2a-2c**) digested in DCl/DMSO-d_6 mixture. Defect linker is ip. H_3O^+ comes from H_2O and HCl contained in DCl.

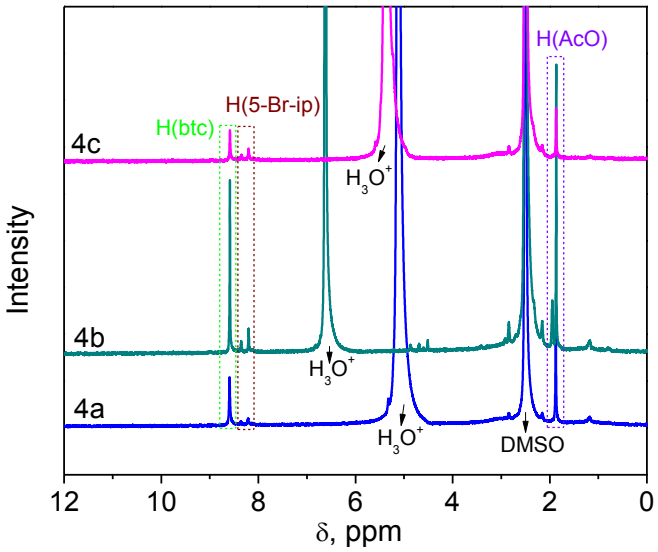

Figure S6. ^{1}H-NMR spectra of the Ru-DEMOFs (**4a-4c**) digested in DCl/DMSO-d_6 mixture. Defect linker is 5-Br-ip. H_3O^+ comes from H_2O and HCl contained in DCl.

Samples of the **3a-3d** series were not possible to digest at the same condition and, therefore, ^{1}H-NMR spectra of these samples have been not collected.

5. Elemental analysis

Table S3. Elemental analysis results (calculated and found) of the activated Ru-DEMOFs (**1a**, **1c** and **1d**) in comparison with the "defect free" parent Ru-MOF. Molar ration of Ru : Cl calculated based on the found mass percentages are also given below.

Sample	C, *wt* %		H, *wt* %		Ru, *wt* %		Cl, *wt* %		Ru : Cl
	cal.	found	cal.	found	cal.	found	cal.	found	
parent	28.5	27.26	2.31	1.65	31.40	30.45	3.67	3.41	3: 1
1a	29.3	28.4	2.28	1.49	31.55	30.08	3.69	3.47	3: 1
1c	31.67	31.26	1.89	1.37	32.03	31.08	3.37	3.27	3: 0.9
1d	30.26	29.43	2.06	1.59	31.36	30.41	3.30	3.35	3: 0.9

Table S4. Proposed formula and the molecule weight of the activated Ru-DEMOFs (**1a**, **1c** and **1d**) as well as the parent Ru-MOF.

Sample	Formula	Molecular weight

parent	$[Ru_3(C_9H_3O_6)_2Cl(CH_3COO)_{0.5}]\cdot(CH_3COOH)_{1.5}(C_9H_6O_6)_{0.1}(H_2O)_4$ $([Ru_3(btc)_2Cl(AcO)_{0.5}]\cdot(AcOH)_{1.5}(H_3btc)_{0.1}(H_2O)_4)$	965.6
1a	$[Ru_3(C_9H_3O_6)_{1.84}(C_8H_3O_5)_{0.16}Cl(OH)_{0.5}]\cdot(CH_3COOH)_{2.8}(H_2O)_2$ $([Ru_3(btc)_{1.84}(5\text{-OH-ip})_{0.16}Cl(OH)_{0.5}]\cdot(AcOH)_{2.8}(H_2O)_2)$	961.1
1c	$[Ru_3(C_9H_3O_6)_{1.36}(C_8H_3O_5)_{0.64}Cl_{0.9}(OH)_{0.6}]\cdot(CH_3COOH)_{2.2}\ (C_8H_6O_5)_{0.4}$ $([Ru_3(btc)_{1.36}(5\text{-OH-ip})_{0.64}Cl_{0.9}(OH)_{0.6}]\cdot(AcOH)_{2.2}\ (5\text{-OH-ip}H_2)_{0.4})$	946.6
1d	$[Ru_3(C_9H_3O_6)_{1.26}(C_8H_3O_5)_{0.74}Cl_{0.9}(OH)_{0.6}]\cdot(CH_3COOH)_{1.3}(C_9H_6O_6)_{0.5}(H_2O)_{2.5}$ $([Ru_3(btc)_{1.26}(5\text{-OH-ip})_{0.74}Cl_{0.9}(OH)_{0.6}]\cdot(AcOH)_{1.3}(H_3btc)_{0.5}(H_2O)_{2.5})$	982.6

The proposed formula of all the samples above have been calculated according to the facts and considerations listed below:

1. Parent (btc) to defect linker (5-OH-ip) ratios have been calculated based on the ^{1}H-NMR spectra (*i.e.*, integration of the linker-related signals) of the respective acid-digested samples.

2. The "defect-free" parent Ru-MOF and reported Ru-DEMOFs are isostructural. At this point it is hard to quantitatively estimate contribution from the defects **B** (missing metal-nodes), therefore, for initial evaluations assumption that the general composition of the prepared solids is $[Ru_3(L)_2Y_y]_n$ (L = total linker amount) was employed. Thus, the Ru : L molar ratio can be taken as a fixed value – 3 : 2. Further, having in mind there is generally 3 molar equivalents of Ru per 1 molecular unit of MOF, the Cl-amount was subsequently calculated based on the measured EA values and respective Ru : Cl ratios.

3. As observed by the ^{1}H-NMR, TG and IR analyses, the contribution of the counter-ions and guest molecules are mainly from Cl, OH, acetate, H_2O and used linkers.
In analogy to the previously reported "defect free" parent Ru-MOF[1] and the Ru-DEMOF with pydc defect linker,[2] in the currently discussed Ru-DEMOFs acetic acid is also present, which is clearly evidenced by the ^{1}H-NMR spectra of the digested samples. To note, the amount of the acetic acid can be considerably reduced by additional solvent exchange procedure, namely, soaking of the activated samples in a large amount of water while intense stirring to exchange the residue acetic acid. However, the risk of leaching out of Ru needs also to be taken into account here.[1] Hence, our current studies dealt with the obtained powders applying gently water soak as solvent exchange procedure to decrease the residue of the acetic acid. And the overall concentration of the acetic acid decreased in comparison with our previously report on the Ru-DEMOF with pydc defect linker in spite of the slightly decrease of Ru content.

In addition of the multiple possible status of acetic acid, starting reactant (*i.e.* linkers) can be also accommodated into the framework as guest molecules or served as counter-ions, since based on the NMR data the amount of the defect linker in some cases appeared to be higher than its respective feeding amount. Besides, minor quantities of the coordinated H_2O might be occluded / resided in the pores as well, as the TG curves of the activated samples show the slight decrease in the range of 100-250 ℃.

Consequently, all these possibilities, especially the situation with acetic acid, obstruct precise evaluation of the exact compositions of the prepared Ru-DEMOFs. Table S4 summarizes the proposed formula of the Ru-DEMOFs (**1a, 1c** and **1d**) which have been estimated based on the listed above considerations and provide the best match with the obtained results of the EA.

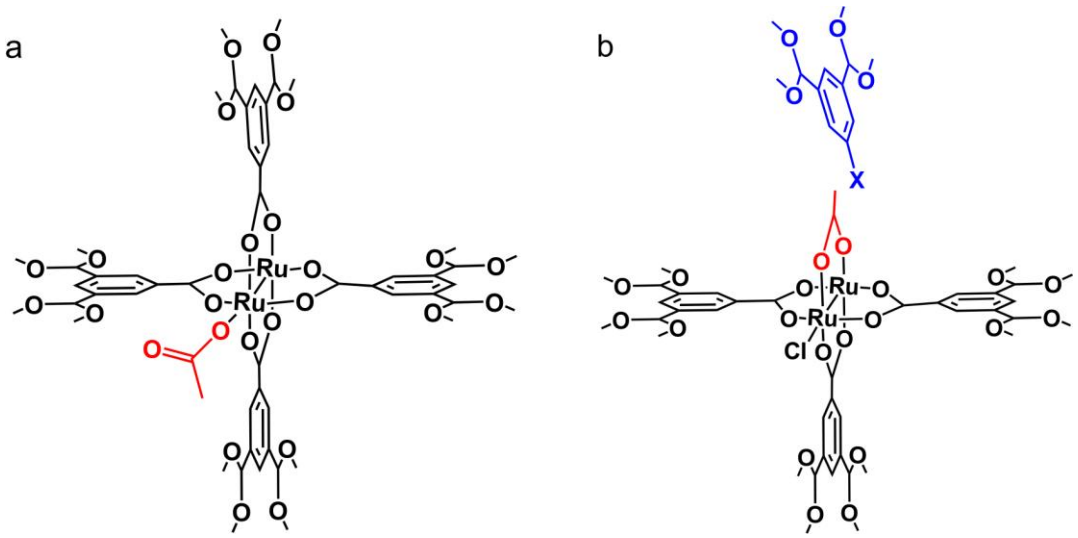

Figure S7. Schematic representation for the two possible origins of acetate in the Ru-DEMOFs.

6. IR spectroscopic analysis

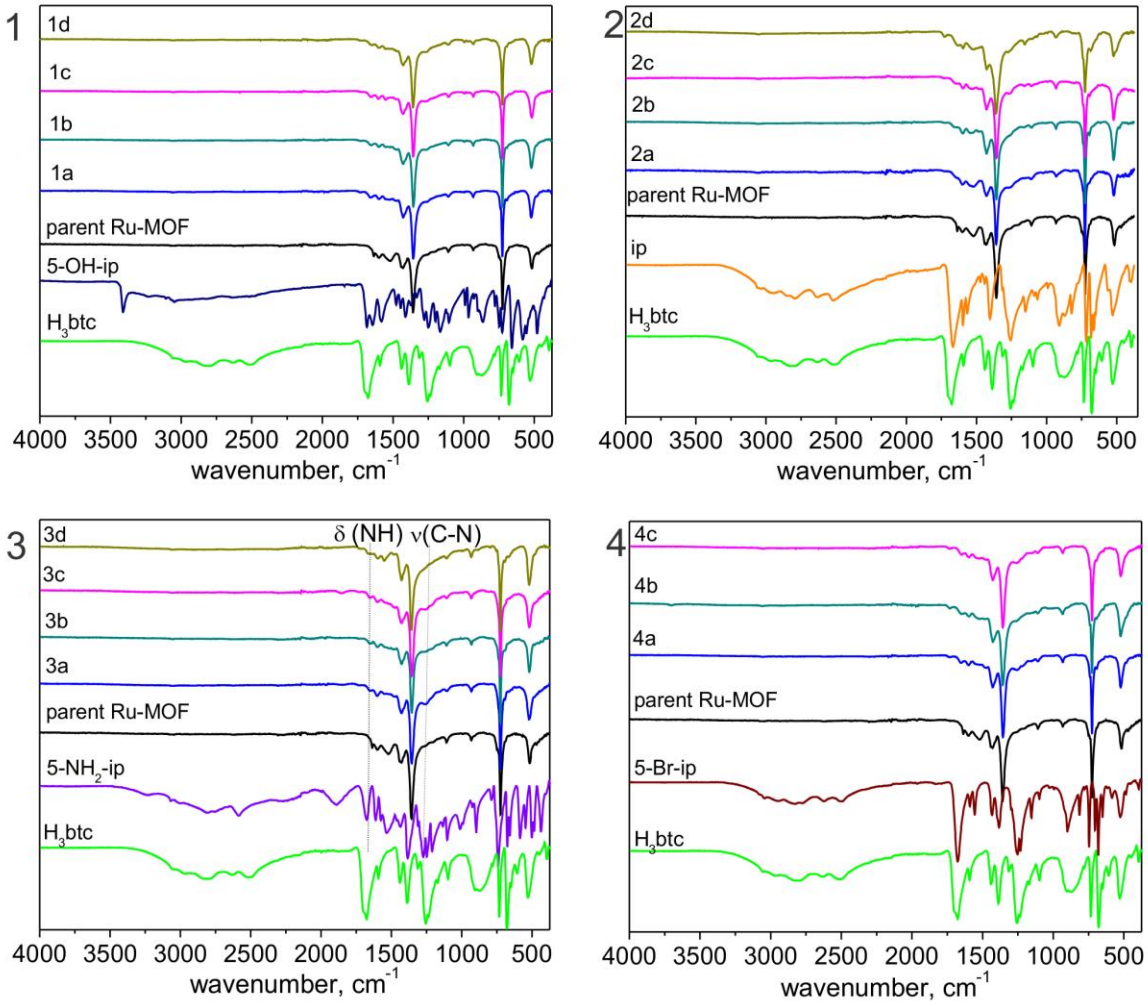

Figure S8. IR spectra of the prepared Ru-DEMOFs **1a-1d** (with 5-OH-ip defect linker)**, 2a-2d** (with ip defect linker)**, 3a-3d** (with 5-NH_2-ip defect linker), **4a-4c** (with 5-Br-ip defect linker) in comparison with the parent Ru-MOF and the corresponding defect linker used in the synthesis, respectively. The vertical dash lines in the Figure S4.3 indicate position of the vibrations of N-H and C-N bonds.

7. EDX spectra

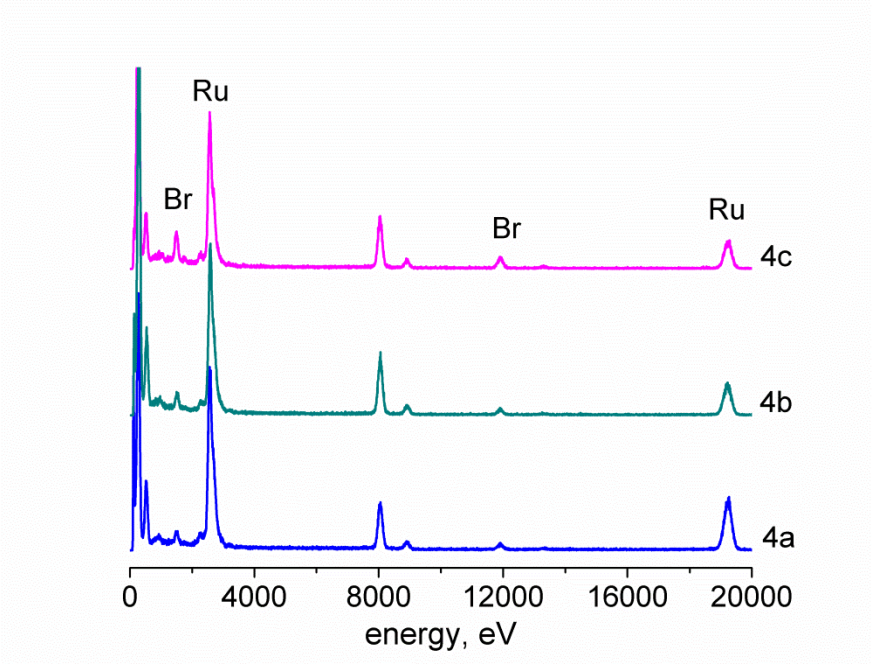

Figure S9. EDX spectra of the Ru-DEMOFs **4a-4c** (with 5-Br-ip defect linker). The detection of Br clearly indicates the presence of the employed defect linker.

8. N_2 sorption at 77K

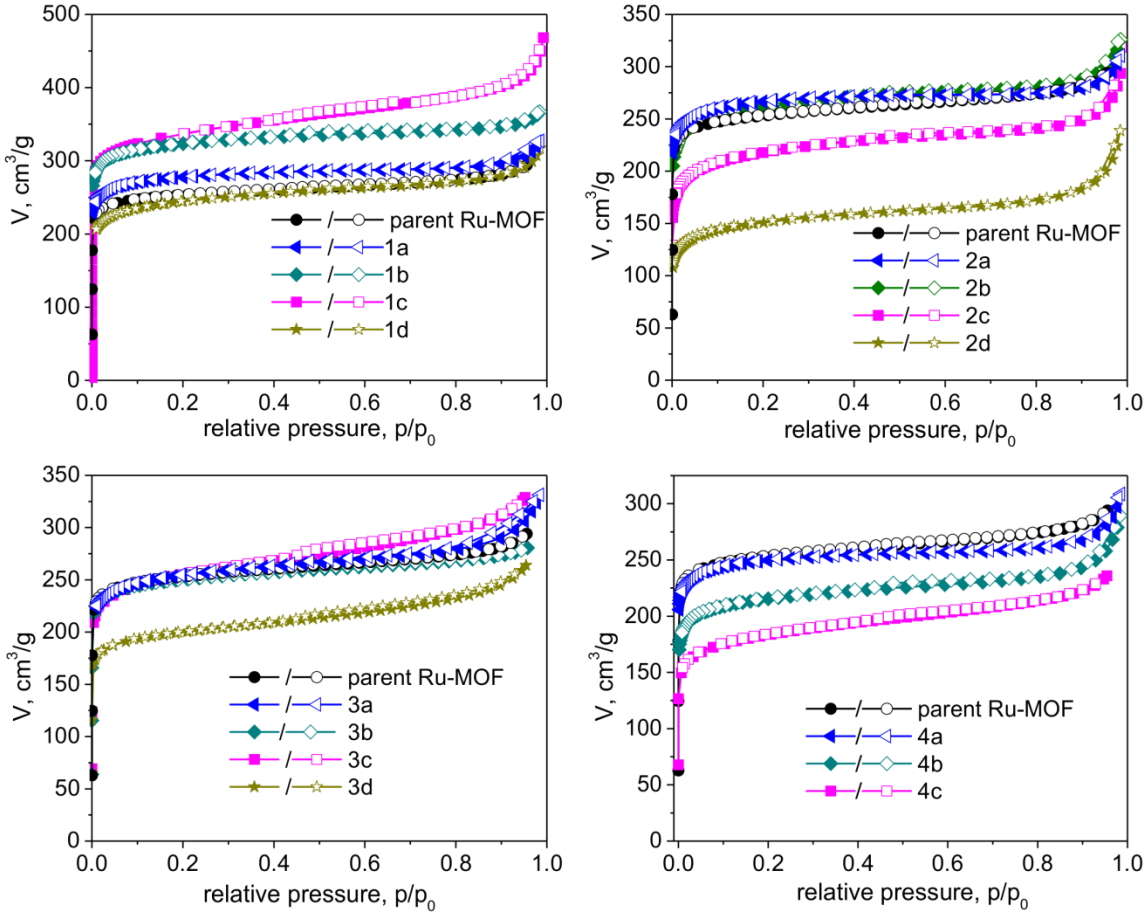

Figure S10. N_2 sorption isotherms collected at 77 K for Ru-DEMOF samples **1a-1d, 2a-2c, 3a-3d, 4a-4c**. **1a-1d**: defect linker is 5-OH-ip, incorporation amount is 8%, 20%, 32% and 37%, respectively; **2a-2c**: defect linker is ip, incorporation amount is 15%,28% and 47%, respectively; **3a-3d**: defect linker is 5-NH_2-ip; **4a-4c**: defect linker is 5-Br-ip, incorporation amount is 17%, 25% and 42%, respectively. Closed and open symbols represent the adsorption and desorption isotherms, respectively. Black circles – parent Ru-MOF; blue triangles – **a** samples of the respective series **1-4**; dark cyan diamonds – **b** samples of the respective series **1-4**; magenta squares – **c** samples of the respective series **1-4**; dark yellow stars – **d** samples of the respective series **1-4**.

Table S5. BET surface area values of the Ru-DEMOFs (**1a-1d**, **2a-2c**, **3a-3d**, **4a-4c**) compared with the parent Ru-MOF.

Sample name	BET surface area, m^2/g	Sample name	BET surface area, m^2/g
Parent Ru-MOF	998	2d	574
1a	1106	3a	1003
1b	1284	3b	985
1c	1302	3c	975
1d	947	3d	781

2a	1059	4a	996
2b	1023	4b	847
2c	838	4c	693

Table S6. BET surface areas of the Ru-DEMOFs **1a**, **1c** and **1d** in comparison with parent Ru-MOF as well as $[Cu_3(btc)_2]_n$. $S_{BET}(m^2/mmol)$ of the Ru-(DE)MOFs was converted from the respective measured $S_{BET}(m^2/g)$ values according to the proposed composition (Table S4).

Sample	$S_{BET}(m^2/g)$	$S_{BET}(m^2/mmol)$
$[Cu_3(btc)_2]_n$	1734[3] 2153*[4]	1049 1301
parent Ru-MOF	998	964
1a (8% of 5-OH-ip)	1106	1062
1c (32% of 5-OH-ip)	1302	1232
1d (37% of 5-OH-ip)	947	930

* theoretical accessible surface area.

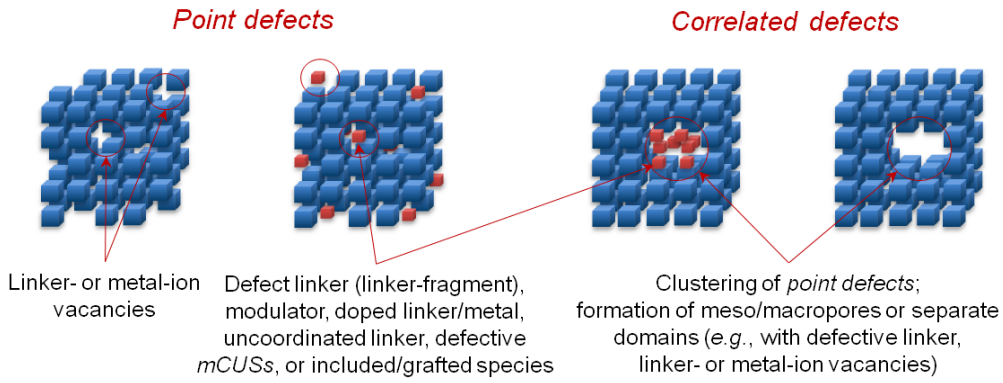

Figure S11. Schematic representation of point defects and correlated defects in DEMOFs.

9. XANES studies

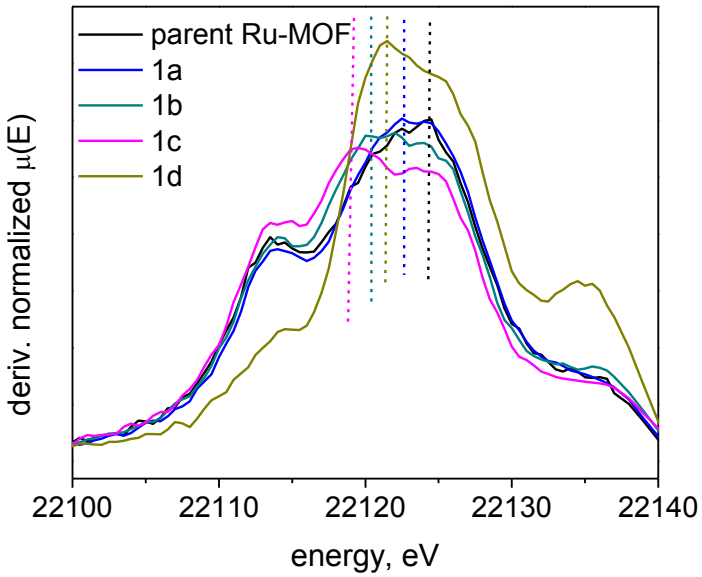

Figure S12. XANES spectra (derivative of the normalized intensity *vs.* Energy) of the Ru-DEMOF materials **1a-1d** compared with the parent Ru-MOF. Black: parent Ru-MOF; blue: **1a** (8% 5-OH-ip); dark cyan: **1b** (20% 5-OH-ip); magenta: **1c** (32% 5-OH-ip); dark yellow: **1d** (37% 5-OH-ip). The dashed vertical line marks the position of the peak calculated from the derivative of the pre-edge jump of each sample.

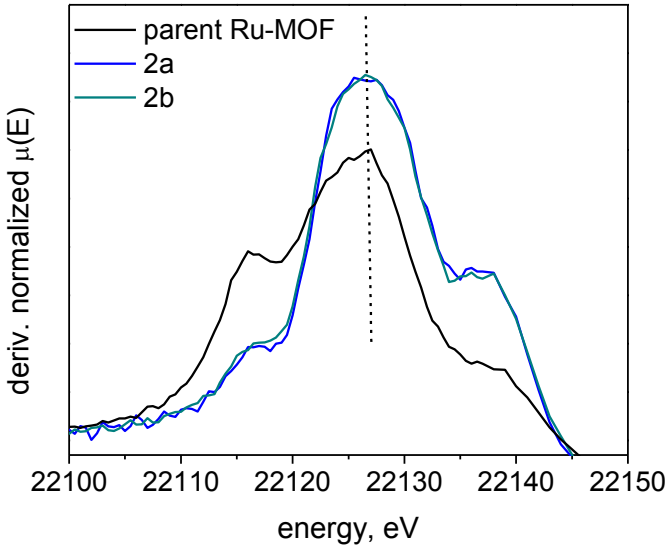

Figure S13. XANES spectra (derivative of the normalized intensity *vs.* Energy) of the Ru-DEMOF materials **2a** and **2b** compared with the parent Ru-MOF. Black: parent Ru-MOF; blue: **2a** (15% ip); dark cyan: **2b** (28% ip). The dashed vertical line marks the position of the peak calculated from the derivative of the pre-edge jump of each sample.

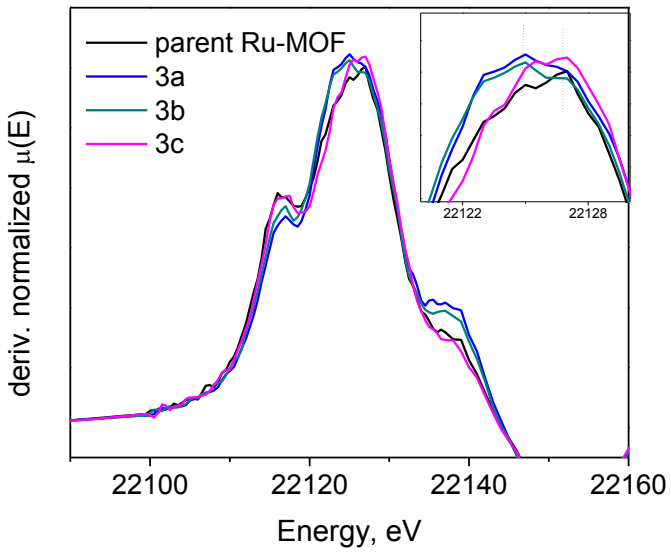

Figure S14. XANES spectra of the parent Ru-MOF and Ru-DEMOFs variants with 5-NH_2-ip defect linker **3a-3c** (derivative of the normalized intensity *vs.* Energy). Zoom of the pre-edge jump position is shown in the upper right corner. Black: parent Ru-MOF; blue: **3a**; dark cyan: **3b**; magenta: **3c**.

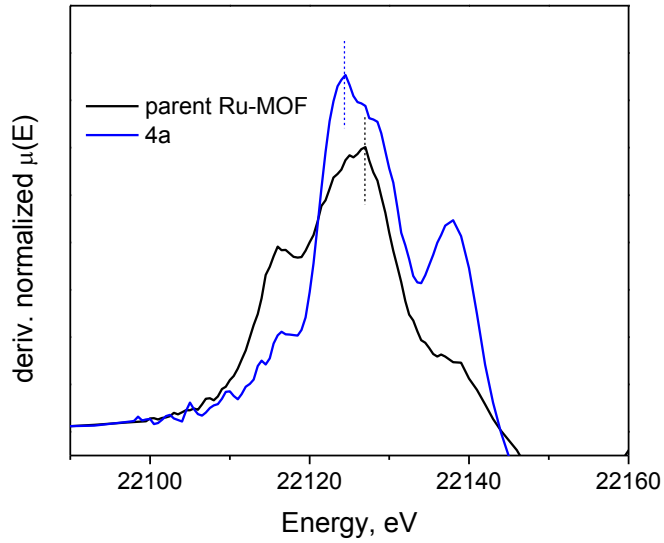

Figure S15. XANES spectra of the parent Ru-MOF and Ru-DEMOF sample **4a** (with 17% 5-Br-ip defect linker, derivative of the normalized intensity *vs.* Energy). Black: parent Ru-MOF; blue: **4a**.

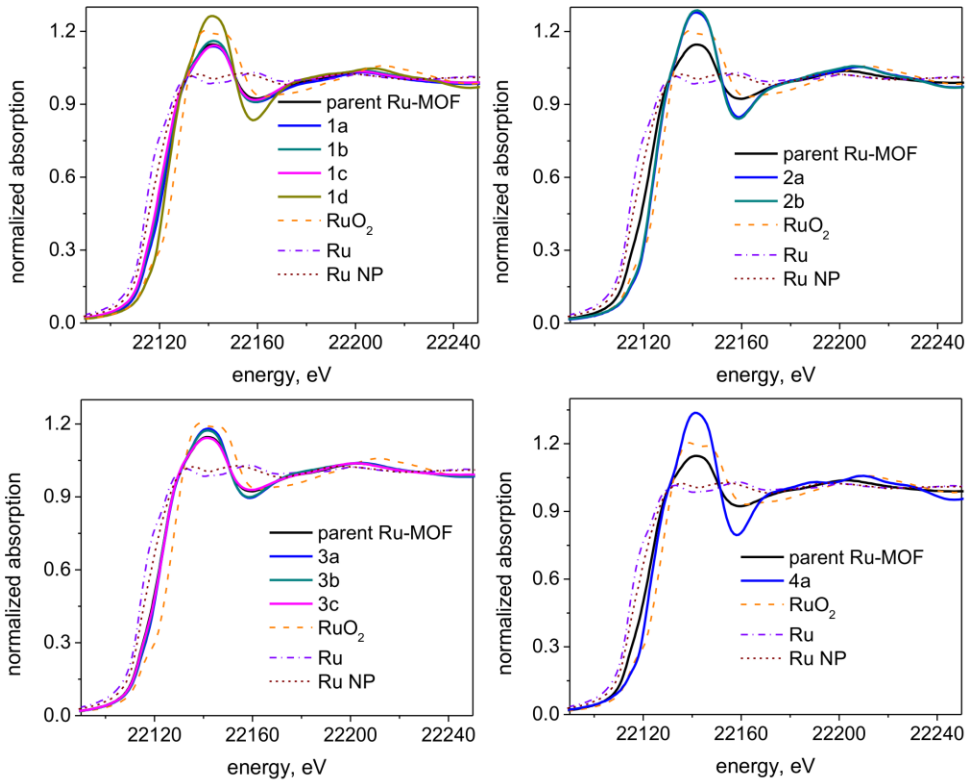

Figure S16. XANES spectra (normalized absorption *vs.* Energy) of the Ru-DEMOF materials (**1a-1d, 2a, 2b, 3a-3c** and **4a**) compared with the parent Ru-MOF as well as some Ru references. Solid Black: parent Ru-MOF; solid blue: **a** samples of the respective series **1-4**; solid dark cyan: **b** samples of the respective series **1-4**; soid magenta: **c** samples of the respective series **1-4**; solid dark yellow: **d** samples of the respective series **1-4**; dash dot violet: Ru; dash orange: RuO_2; short dash wine: Ru nano-particles(NP).

10. XPS study

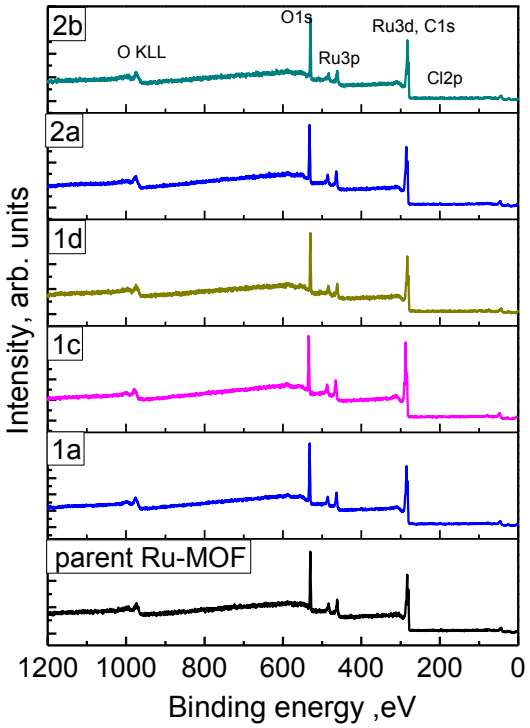

Figure S17. XPS survey scan of the parent Ru-MOF and Ru-DEMOFs (**1a, 1c, 1d, 2a** and **2b**). **1a, 1c** and **1d** - 8%, 32% and 37% 5-OH-ip incorporation, respectively; **2a** and **2b** - 15% and 28% ip incorporation, respectively.

Table S7 The assignments of binding energies as well as the ratio of Ru^{3+} / Ru^{2+}/ $Ru^{\delta+}$ (calculated from the deconvoluted spectra) in the parent Ru-MOF sample and Ru-DEMOFs (**1a, 1c 1d, 2a** and **2b**). **1a, 1c** and **1d** - 8%, 32% and 37% of 5-OH-ip, respectively; **2a** and **2b** - 15% and 28% of ip, respectively.

Sample	Binding energy, eV	Assignment	Ru^{3+} / Ru^{2+}/ $Ru^{\delta+}$ ratio
Parent Ru-MOF	285.86 / 281.66	Ru^{2+}	1 / 1.24 / -*
	286.86 / 282.66	Ru^{3+}	
1a	285.86 / 281.66	Ru^{2+}	1 / 1.75 / 0.08
	286.86 / 282.66	Ru^{3+}	
	284.65 / 280.45	$Ru^{\delta+}$	
1c	285.71 /281.51	Ru^{2+}	1 / 1.69 / 0.59
	286.71 / 282.60	Ru^{3+}	
	284.60 / 280.40	$Ru^{\delta+}$	
1d	285.72 / 281.52	Ru^{2+}	1 / 1.23 / 0.09
	286.72 / 282.52	Ru^{3+}	
	284.65 / 280.45	$Ru^{\delta+}$	

2a	285.86 /281.66	Ru^{2+}	1 / 1.73/ -*
	286.86 / 282.66	Ru^{3+}	
2b	285.88 / 281.68	Ru^{2+}	1 / 1.42 / -*
	286.88 / 282.76	Ru^{3+}	

* no species have been determined.

11. UHV-IR spectra recorded during CO and CO_2 dosing

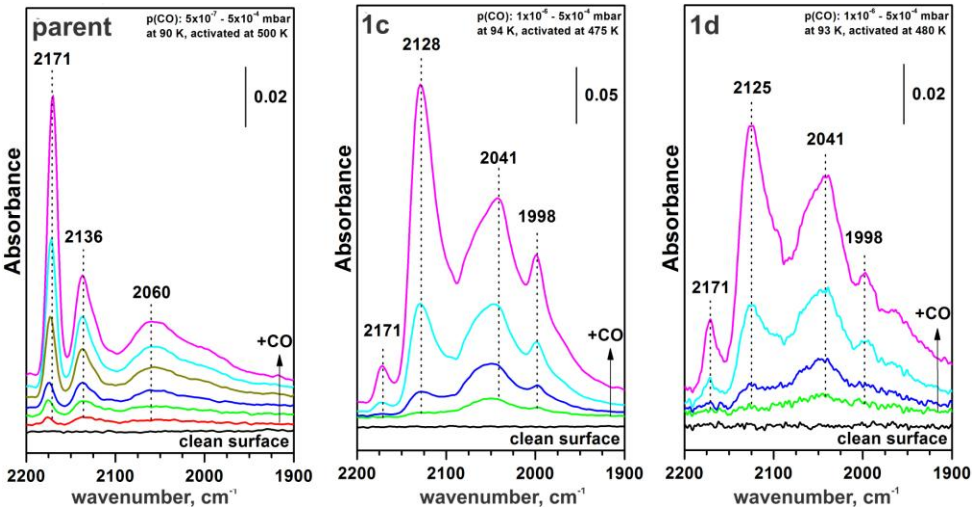

Figure S18. UHV-IR spectra of the parent Ru-MOF and Ru-DEMOFs (**1c** and **1c)** with 5-OH-ip defect linker (from left to right) upon CO dosing (p(CO): 5×10^{-7} - 5×10^{-4} mbar) collected at 90-94 K after annealing at 475 - 500 K. **1c** - 32%, **1d** - 37% incorporation of defect linker. The broad absorption bands between 2100 cm^{-1} and 1900 cm^{-1} in the parent Ru-MOF indicate some inherent defects that cannot be avoided during the crystal formation.

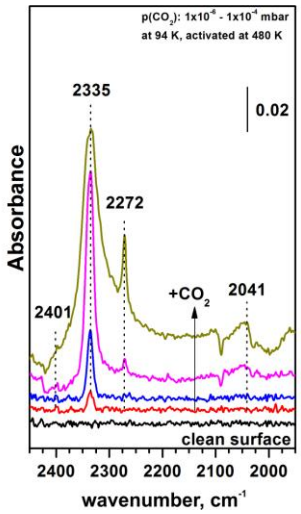

Figure S19. UHV-IR spectra of Ru-DEMOF **1d** upon CO_2 dosing collected at 94 K after annealing at 480 K.

Table S8. Possible defect combinations in the prepared Ru-DEMOFs according to the conducted XANES, UHV-IR and XPS studies.

Sample	Assumption I	Assumption II
5-OH-ip defect linker		
1a	defects**A*** + **B**	defects **A***
1c	defects **A***** + **B**	defects **A*****
1d	defects **A*** + **B**	defects **A*** + **B**
ip defect linker		
2a	defects **B**	
2b	defects **B**	
5-NH_2-ip defect linker		
3a	defects **A**** + **B**	defects **A****
3b	defects **A***** + **B**	defects **A*****
3c	defects **A*** + **B**	defects **A*** + **B**
5-Br-ip defect linker		
4a	defects **A** + **B**	defects **A**

* expresses relative defects concentration.

The arrangement of the two defect types in Ru-DEMOFs (**1a, 1c** and **1d**) is rather diverse. Still, based on the information on XANES and UHV-IR with CO probing, we can assume two possibilities: I) both **defects** of **type A** and **B** might be generated in the Ru-DEMOFs (**1a-1d**) with the incorporation of 5-OH-ip. The **defects** of **type A** are much more competitive and became gradually dominant in case of the lower doping (samples **1a** (8%) and **1c** (32%)). Along with increase of doping level (**1d**, 37%) of 5-OH-ip, the dominant effect of **defects** of **type A** is substituted slowly by the **defects** of **type B**; II) the **defects** of **type A** are generated and becomes gradually dominant in case of relatively low doping (samples **1a** and **1c**). Afterwards, **defects** of **type B** are created simultaneously when the doping level reaches 37% in case of **1d**. Therefore, the influence caused by the **defects** of **type A** could be partly eliminated. Nevertheless, both assumptions indicate that the **defects** of **type A** play a major role in Ru-DEMOFs **1c** (32% of 5-OH-ip). A comprehensive table summarizing possible defect combinations in the particular Ru-DEMOFs (based on the performed analyses) is given above (Table S8).

Figure S20. Other possible defect fragments in the structure of Ru-DEMOFs. a. Two defect linkers (*DL*) and two btc in a fragment of modified paddlewheel b. Two defect linkers and two Hbtc in a fragment of missing node. Free carboxylates of Hbtc were bound with each other via hydrogen bounds. c. Correlated modified paddlewheel and missing paddlewheel.

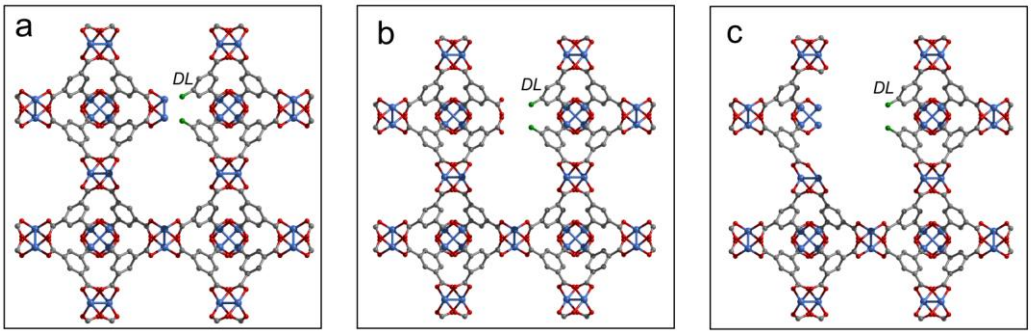

12. Sorption of small molecules (*i.e.*, CO, H_2 and CO_2)

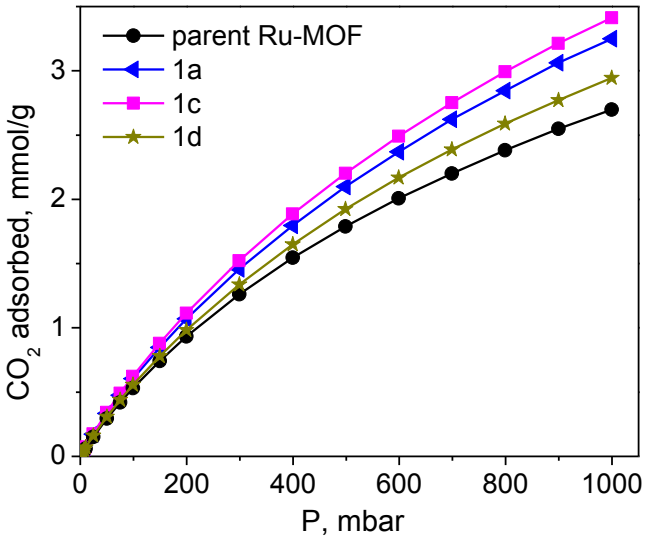

Figure S21. CO_2 isotherms collected at 298 K for the parent Ru-MOF and DEMOF derivatives **1a** (8%), **1c** (32%) and **1d** (37%) with 5-OH-ip defect linker. Black circles – parent Ru-MOF; blue triangles – **1a**; magenta squares – **1c**; dark yellow stars – **1d**.

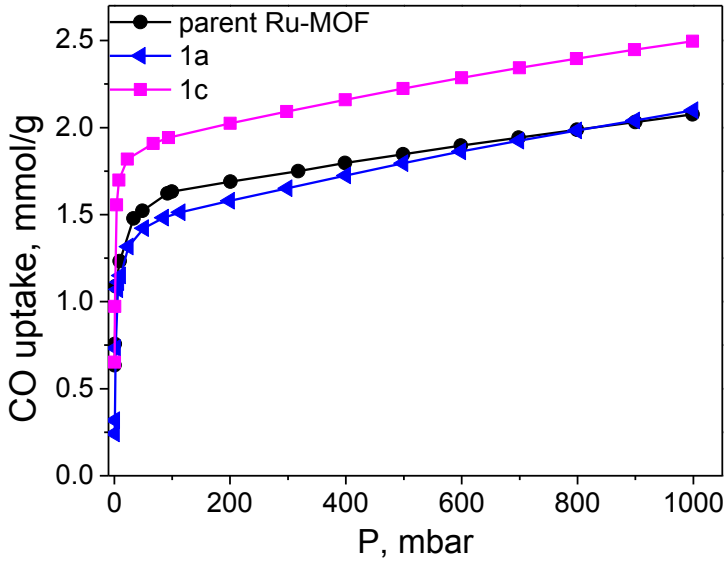

Figure S22. CO isotherms measured at 298 K for the parent Ru-MOF and Ru-DEMOF samples **1a** (8%) and **1c** (32%) with 5-OH-ip defect linker. Black circle – parent Ru-MOF; blue triangles – **1a**; magenta squares – **1c**.

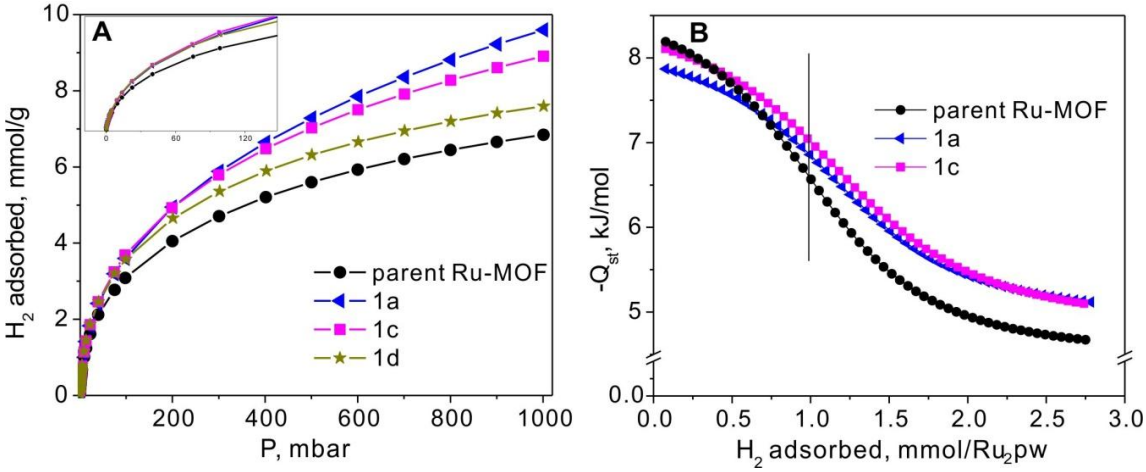

Figure S23. A. H_2 isotherms measured at 77 K for the parent Ru-MOF and DEMOFs **1a** (8%)**, 1c** (32%) and **1d** (37%) with 5-OH-ip defect linker. Black circles – parent Ru-MOF; blue triangles – **1a**; magenta squares – **1c**; dark yellow stars – **1d**. B. Isosteric heats of adsorption of **1a** and **1c** calculated from the H_2 adsorption isotherms at 77K and 87K. The vertical line stands for the position where one H_2 molecule is absorbed per Ru_2-paddlewheel.

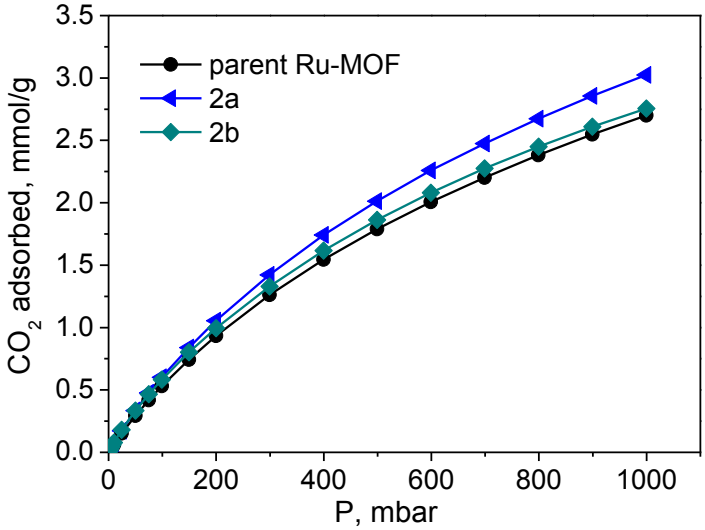

Figure S24. CO_2 isotherms collected at 298 K for the parent Ru-MOF and DEMOF derivatives **2a** (15%) and **2b** (28%) with ip defect linker. Black circles – parent Ru-MOF; blue triangles – **2a**; dark cyan diamonds – **2b**.

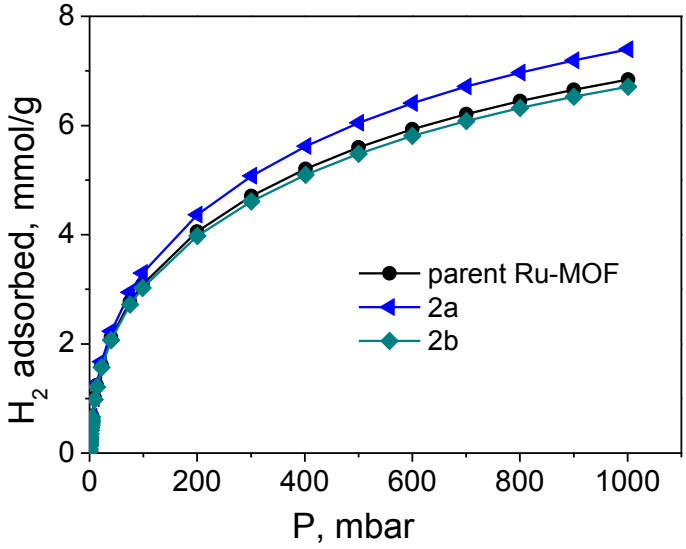

Figure S25. H_2 isotherms measured at 77 K for the parent Ru-MOF and its derivatives **2a** (15%) and **2b** (28%) with ip defect linker. Black circles – parent Ru-MOF; blue triangles – **2a**; dark cyan diamonds – **2b**.

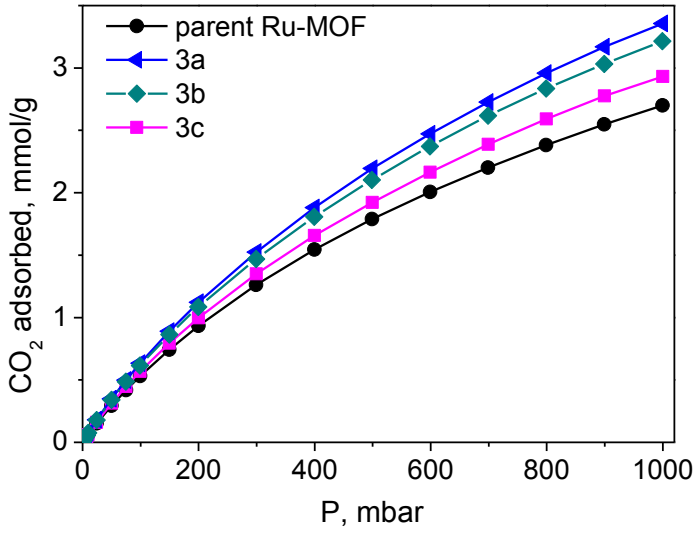

Figure S26. CO_2 isotherms collected at 298 K for the parent Ru-MOF and its derivatives **3a**, **3b** and **3c** with 5-NH_2-ip defect linker. Black circles – parent Ru-MOF; blue triangles – **3a**; dark cyan diamonds – **3b**; magenta squares – **3c.**

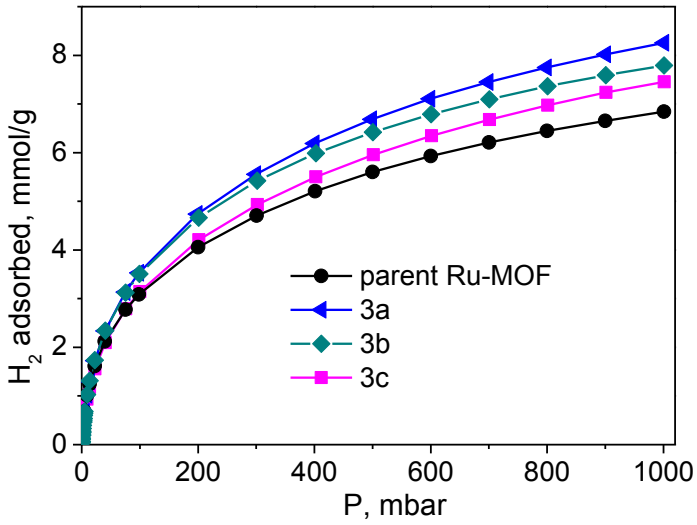

Figure S27. H_2 isotherms collected at 77 K for the parent Ru-MOF and its derivatives **3a**, **3b** and **3c** with 5-NH_2-ip defect linker. Black circles – parent Ru-MOF; blue triangles – **3a**; dark cyan diamonds – **3b**; magenta squares – **3c.**

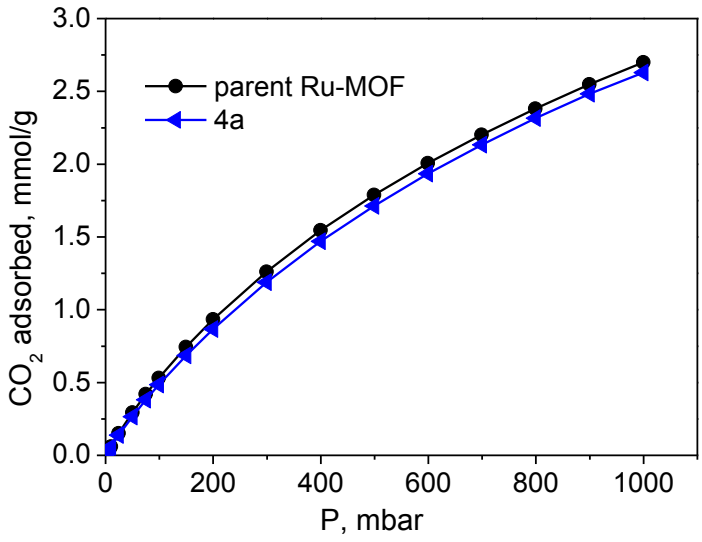

Figure S28. CO_2 isotherms measured at 298 K for the parent Ru-MOF and Ru-DEMOF **4a** (17%) with 5-Br-ip defect linker. Black circles – parent Ru-MOF; blue triangles – **4a**.

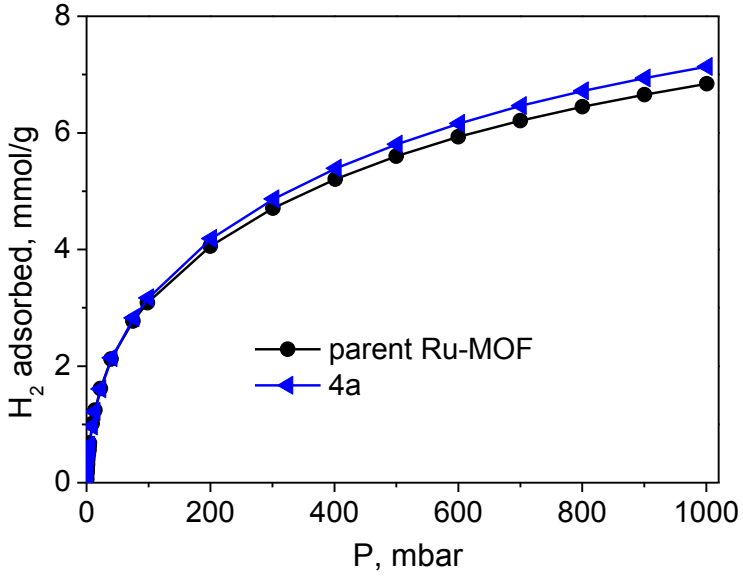

Figure S29. H_2 isotherms measured at 77 K for the parent Ru-MOF and Ru-DEMOF **4a** (17%) with 5-Br-ip defect linker. Black circles – parent Ru-MOF; blue triangles – **4a**.

Table S9. H_2 (77 K) and CO_2 (298 K) uptakes for the parent Ru-MOF and its defect-engineered variants **1a, 1c, 1d, 2a, 2b, 3a-3c** and **4a** at 1000 mbar. **1:** defect linker is 5-OH-ip; **2:** defect linker is ip; **3**: defect linker is 5-NH_2-ip; **4**: defect linker is 5-Br-ip.

Sample name	CO_2 uptake (mmol/g)	H_2 uptake (mmol/g)
Parent Ru-MOF	2.7	6.8

1a	3.2	9.6
1c	3.4	8.9
1d	2.9	7.6
2a	3.0	7.4
2b	2.8	6.7
3a	3.4	8.3
3b	3.2	7.8
3c	2.9	7.4
4a	2.6	7.1

13. Catalytic tests

Table S10. The conversion of ethylene to butene in toluene under different conditions.

Entry	Catalyst (mg)	Temperature (°C)	Time (h)	Additive	TOF (h^{-1})
1	**1c** (2.5)	80	24	----	0.92
2	**1c** (2)	80	1	Et_2AlCl	4.38
3	**1c** (2)	80	1	----	0.88
4	**1c** (2.4)	26	2	Et_2AlCl	2.15
5	**1c** (2.1)	80	2	Et_2AlCl	4.36
6	**1a** (2)	80	2	Et_2AlCl	2.3
7	Parent Ru-MOF (1.8)	80	2	Et_2AlCl	2.05

Table S11. Comparison of the yields of pyrrole and TOF values after 4 h in the Paal-Knorr reaction for different Ru-DEMOF samples as well as the parent Ru-MOF (used as a reference).

Sample	Ru content (mol %)	yield at 4h, %	TOF(h^{-1})*
Parent Ru-MOF	2	48	6.17
1a	2	77	9.83
1b	2	73	9.25
1c	2	65	8.17
1d	2	58	7.25
2a	2	82	10.36
2b	2	57	7.09

blank	-	28	-

* TOF value was calculated by mol of product (mol of Ru)$^{-1}$ h^{-1}. For easier comparison the molecule weight (M_w) used for calculation here is based on the ideal model compound without any guest molecules. Namely, for parent Ru-MOF- $Ru_3(C_9H_3O_6)2Cl_{1.5}$, M_w=771 g/mol; **1a**- $Ru_3(C_9H_3O_6)_{1.84}(C_8H_4O_5)_{0.16}Cl_{1.5}$, 766 g/mol; **1b**- $Ru_3(C_9H_3O_6)_{1.6}(C_8H_4O_5)_{0.4}Cl_{1.5}$, 760 g/mol, **1c**- $Ru_3(C_9H_3O_6)1.4(C_8H_4O_5)0.6Cl_{1.5}$, 754 g/mol; **1d**- $Ru_3(C_9H_3O_6)_{1.24}(C_8H_4O_5)0.76Cl_{1.5}$, 750 g/mol; **2a**- $Ru_3(C_9H_3O_6)_{1.7}(C_8H_4O_4)_{0.3}Cl_{1.5}$, 758 g/mol, **2b,** $Ru_3(C_9H_3O_6)_{1.44}(C_8H_4O_4)_{0.56}Cl_{1.5}$, 746 g/mol.

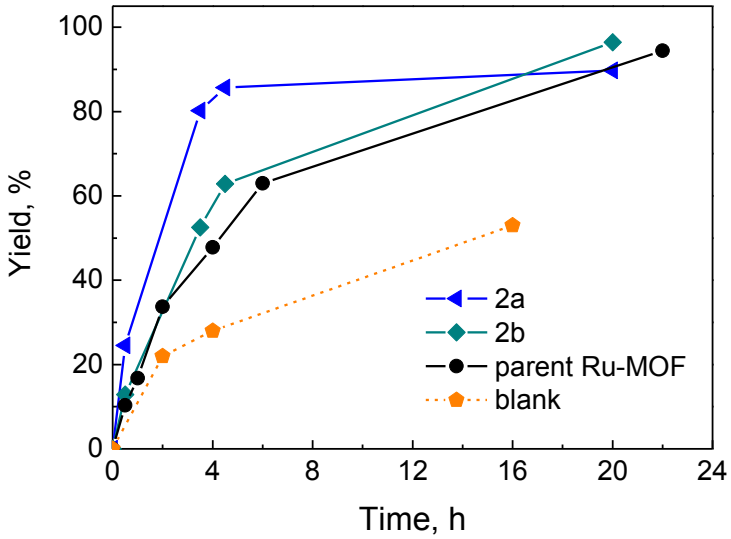

Figure S30. Time-yield plot of Paal-Knorr synthesis of phenylamine reacting with 2,5-hexadione, giving the pyrrol using Ru-DEMOFs **2a (**15% ip incorporation) and **2b** (28% ip incorporation) as catalysts in comparison with the parent Ru-MOF. Blank stands for the experiment where on catalyst was added into the reaction mixture.

[1] W. Zhang, O. Kozachuk, R. Medishetty, A. Schneemann, R. Wagner, K. Khaletskaya, K. Epp, R. A. Fischer, *Eur. J. Inorg. Chem.* **2015**, *2015*, 3913-3920.

[2] O. Kozachuk, I. Luz, F. X. Llabrés i Xamena, H. Noei, M. Kauer, H. B. Albada, E. D. Bloch, B. Marler, Y. Wang, M. Muhler, R. A. Fischer, *Angew. Chem. Int. Ed.* **2014**, *53*, 7058-7062.

[3] C. R. Wade, M. Dinca, *Dalton Trans.* **2012**, *41*, 7931-7938.

[4] T. Düren, F. Millange, G. Férey, K. S. Walton, R. Q. Snurr, *J. Phys. Chem. C* **2007**, *111*, 15350-15356.